Manganese Indicates a Transition from Sub- to Near-Chandrasekhar Type Ia Supernovae in Dwarf Galaxies*

Mithi A. C. de los Reyes 6. Evan N. Kirby 6. Ivo R. Seitenzahl 6. and Ken J. Shen 6.

Department of Astronomy, California Institute of Technology 1200 E. California Blvd., MC 249-17 Pasadena, CA 91125, USA; mdelosre@caltech.edu

School of Science, University of New South Wales, Australian Defence Force Academy Canberra, ACT 2600, Australia

Department of Astronomy and Theoretical Astrophysics Center, University of California Berkeley, CA 94720, USA

Received 2019 October 11; revised 2020 February 4; accepted 2020 February 5; published 2020 March 6

Abstract

Manganese abundances are sensitive probes of the progenitors of Type Ia supernovae (SNe Ia). In this work, we present a catalog of manganese abundances in dwarf spheroidal satellites of the Milky Way, measured using medium-resolution spectroscopy. Using a simple chemical evolution model, we infer the manganese yield of SNe Ia in the Sculptor dwarf spheroidal galaxy (dSph) and compare to theoretical yields. The sub-solar yield from SNe Ia ([Mn/Fe]_{Ia} = $-0.30^{+0.03}_{-0.03}$ at [Fe/ H] = -1.5 dex, with negligible dependence on metallicity) implies that sub-Chandrasekhar-mass (sub- $M_{\rm Ch}$) white dwarf progenitors are the dominant channel of SNe Ia at early times in this galaxy, although some fraction ($\gtrsim 20\%$) of $M_{\rm Ch}$ Type Ia or Type Iax SNe are still needed to produce the observed yield. First-order corrections for deviations from local thermodynamic equilibrium increase the inferred [Mn/Fe]_{Ia} by as much as ~ 0.3 dex. However, our results also suggest that the nucleosynthetic source of SNe Ia may depend on environment. In particular, we find that dSphs with extended star formation histories (Leo I, Fornax dSphs) appear to have higher [Mn/Fe] at a given metallicity than galaxies with early bursts of star formation (Sculptor dSph), suggesting that $M_{\rm Ch}$ progenitors may become the dominant channel of SNe Ia at later times in a galaxy's chemical evolution.

Unified Astronomy Thesaurus concepts: Dwarf spheroidal galaxies (420); Dwarf galaxies (416); Sculptor dwarf elliptical galaxy (1436); Type Ia supernovae (1728); Chemical abundances (224); Galaxy abundances (574); Stellar abundances (1577)

Supporting material: machine-readable tables

1. Introduction

Type Ia supernovae (SNe Ia) have long been understood to be the thermonuclear explosions of white dwarfs (WDs). Their ability to be empirically normalized to the same peak luminosity (e.g., Phillips 1993) has made them indispensible astrophysical tools as "standardizable candles" for measuring cosmological distances. Indeed, SNe Ia were used in the Nobel Prize-winning discovery of the accelerating expansion of the universe (Riess et al. 1998; Perlmutter et al. 1999).

However, the fundamental physics governing SNe Ia—particularly the actual explosion mechanism—is still poorly constrained. The traditional paradigm of SNe Ia suggests that a thermonuclear supernova occurs when a single WD accretes material from a non-degenerate companion star and undergoes runaway thermonuclear burning near the Chandrasekhar mass of $M_{\rm Ch} \approx 1.4 \, M_{\odot}$.

Several problems persist with this paradigm. Simulated detonations of a $M_{\rm Ch}$ WD tend to underproduce intermediatemass elements (IMEs) such as silicon and sulfur that dominate observed SNe Ia light curves (e.g., Arnett et al. 1971). Near-Chandrasekhar mass WDs also appear to be rare (e.g., Giammichele et al. 2012; Tremblay et al. 2016), and increasing the mass of an accreting WD can be challenging (e.g., Shen & Bildsten 2007; Maoz et al. 2014). Finally, this physical mechanism requires accretion from a companion star, but

multiple nearby SNe Ia have been observed without companions. For instance, radio and X-ray data from SN2011fe in M101 strongly disfavor the existence of a non-degenerate companion star (Margutti et al. 2012; Pérez-Torres et al. 2014).

Various models have attempted to resolve some of these discrepancies, largely by tweaking the assumptions of a *prompt detonation* of a *single* WD at the Chandrasekhar limit. For example, if a $M_{\rm Ch}$ WD is allowed to expand before detonation instead of promptly detonating, the expansion will produce low-density regions. These regions then provide ideal conditions for the nucleosynthesis of the missing IMEs (Seitenzahl & Townsley 2017). One way to achieve this scenario is by prolonging the explosion with the so-called "deflagration-to-detonation transition" (DDT) (Khokhlov 1991).

Alternatively, the rarity of $>1~M_{\odot}$ WDs suggests that many, if not most, SNe Ia are produced by the explosions of lowermass WDs. One of the most favored models for exploding a single sub- $M_{\rm Ch}$ WD is the "double-detonation" model, in which the WD accretes helium from a He-rich companion, such as a non-degenerate He star. The He shell may detonate when it becomes massive enough, sending shocks through the WD that explode it (Nomoto 1982; Woosley et al. 1986; Livne 1990). This model can successfully reproduce most observations of typical SNe Ia, including the nucleosynthesis of IMEs (e.g., Woosley & Kasen 2011).

Finally, a sub- $M_{\rm Ch}$ WD can also explode if it has a second WD companion. This "double-degenerate" channel may account not only for the rarity of massive WDs and the expected nucleosynthesis of IMEs, but also for the missing companion stars near some observed SNe Ia. Physically, a

^{*} The data presented herein were obtained at the W. M. Keck Observatory, which is operated as a scientific partnership among the California Institute of Technology, the University of California and the National Aeronautics and Space Administration. The Observatory was made possible by the generous financial support of the W. M. Keck Foundation.

double-degenerate explosion may be similar to the double-detonation model described above, in which the primary WD accretes from a secondary He WD (e.g., Shen et al. 2018b). This model has been invoked to explain the discovery of hypervelocity WDs, which are thought to be surviving donor companions of these "dynamically driven, double-degenerate, double-detonation" explosions (Shen et al. 2018a). Alternatively, binary sub- $M_{\rm Ch}$ WDs can merge, form a super- $M_{\rm Ch}$ remnant, and undergo a DDT (Iben & Tutukov 1984; Webbink 1984).

The abundances of elements produced by SNe Ia can be used to distinguish between these physical models. While these abundances can be measured directly in spectra of SNe or SN remnants, these direct observations are inherently limited by the rarity of SNe Ia, and many abundances are difficult to determine from direct spectroscopy. The focus of this paper is to instead indirectly infer nucleosynthetic yields from ancient stars, because the abundances of these stars are linked to the chemical evolution of a galaxy.

1.1. Measuring Nucleosynthesis with Dwarf Galaxies

The chemical evolution of a galaxy is largely driven by enrichment from SNe. Core-collapse SNe (CCSNe) are driven by the deaths of the most massive stars in a galaxy, which begin very early in a galaxy's history. SNe Ia, on the other hand, can only begin to explode much later, after lower-mass stars die and create WDs.

Both SNe Ia and CCSNe produce iron (Fe). Throughout the lifetime of a galaxy, SNe will therefore produce an increase in the overall abundance of Fe, [Fe/H].⁴ However, because SNe Ia and CCSNe have different nucleosynthetic products, the abundance of other elements relative to Fe will change once SNe Ia begin to explode. In particular, since dwarf spheroidal (dSph) galaxies have low star formation rates, their chemical evolution is dominated at late times by SNe Ia rather than by CCSNe. As [Fe/H] increases over time, the relative abundance of an element relative to Fe will approach the SN Ia yield. The yields of various elements can then be used to infer properties of SNe Ia alone (McWilliam et al. 2018).

Furthermore, the abundance contributions specifically from SNe Ia (f_{Ia}) can be computed using the well-constrained theoretical yields of various elements from CCSNe. Once the SNe Ia yields are disentangled from CCSNe yields, measurements of different elemental abundances can be used to infer properties of SNe Ia alone. Kirby et al. (2019) originally performed this analysis for several Fe-peak elements (Cr. Co, Ni), fitting a simple chemical decomposition model to determine f_{Ia} and measure the absolute SN Ia yields of these elements. These yields suggested that sub- $M_{\rm Ch}$ WDs are the dominant progenitors of SNe Ia in dwarf galaxies at early times. Kirby et al. (2019) also found that galaxies with star formation lasting for several Gyr have higher [Ni/Fe] abundances than galaxies with an early burst of star formation, potentially indicating that the dominant SN Ia channel depends on star formation history (SFH).

1.2. Manganese

In this work, we aim to extend the analysis of Kirby et al. (2019) to manganese (Mn), which is a particularly sensitive probe of the physics of SNe Ia (Seitenzahl et al. 2009, 2013a, 2015). Like the other Fe-peak elements, the production of Mn is dominated by Type Ia rather than CCSNe. Furthermore, the only stable isotope of Mn, ⁵⁵Mn, is produced via nucleosynthetic pathways that are strongly dependent on the density of the progenitor WD.

Nearly all ⁵⁵Mn is produced as its radioactive parent nucleus ⁵⁵Co, which can be produced in low entropy ("normal") freeze-out from nuclear statistical equilibrium at densities $\rho \gtrsim 2 \times 10^8$ g cm⁻³ (Seitenzahl & Townsley 2017). Higher yields of ⁵⁵Co and therefore ⁵⁵Mn can be achieved if silicon does not completely burn, while lower yields can be achieved at high entropy and low density, where the presence of protons during "alpha-rich" freeze-out ultimately destroys ⁵⁵Co via the reaction ⁵⁵Co(p, γ) ⁵⁶Ni (Seitenzahl et al. 2013a). In WDs well below $M_{\rm Ch}$, ⁵⁵Co is generally produced at densities below nuclear statistical equilibrium, producing lower yields of ⁵⁵Mn.

In other words, stable Mn is more likely to be synthesized in near- $M_{\rm Ch}$ WDs than in sub- $M_{\rm Ch}$ progenitors. The observed yield of Mn from SNe Ia is therefore physically significant—higher yields suggest $M_{\rm Ch}$ explosions, while lower yields may indicate sub- $M_{\rm Ch}$ models. To that end, there is significant interest in measuring stellar Mn abundances.

Previous works have presented conflicting results of Mn measurements in nearby dSphs. North et al. (2012) compiled literature Mn abundances and used high-resolution spectroscopy to measure additional Mn abundances for stars in Sculptor (N = 50) and Fornax (N = 60) dSphs. They concluded that the Mn abundances imply sub-solar [Mn/Fe] ratios, and that the specific trend of [Mn/Fe] versus [Fe/H] implies a metallicity-dependent Mn yield from SNe Ia. However, the North et al. (2012) measurements used high-resolution spectroscopy and were largely limited to higher-metallicity stars ([Fe/H] $\gtrsim -1.75$), making it difficult to precisely constrain the trend of [Mn/Fe] across lower [Fe/H].

On the other hand, Kobayashi et al. (2015) used a different sample to suggest that high Mn abundances point to dense SNe Ia, and that a special class of near- $M_{\rm Ch}$ "Type Iax" SNe are needed to produce enough Mn to match observations. Cescutti & Kobayashi (2017) made a similar argument for a combination of "normal" and "Iax" SNe using Mn abundances for N=20 stars in the dSph Ursa Minor. In both studies, the observations are too incomplete to draw any significant conclusions.

In this paper, we increase the sample size and parameter space of these literature Mn abundances by using medium-resolution spectroscopy (MRS) to extend to fainter and more metal-poor stars in dSph galaxies. We then use these measurements to distinguish between different SNe Ia models. Our observations are described in Section 2. In Section 3, we describe our pipeline for measuring Mn abundances, validate our measurement technique using globular clusters, and present Mn abundances for stars in classical dSph galaxies. We use a simple chemical evolution model to infer Mn yields from SNe Ia in Section 4 before discussing the implications for SN Ia physics in Section 5. Finally, we summarize our conclusions in Section 6.

⁴ Throughout this paper, we use bracket abundances referenced to solar (e.g., $[Fe/H] = \log_{10}(n_{Fe}/n_H)_* - \log_{10}(n_{Fe}/n_H)_{\odot})$, where n_X is the atomic number density of X. Solar abundances are adopted from Asplund et al. (2009).

Table 1 Spectroscopic Targets

Object	R.A. (J2000)	Decl. (J2000)	Dist. (kpc)	Slitmask	$N_{\rm stars}$	Date	Airmass	Seeing (")	Exposures (s)
				Globular	Clusters				
M53 (NGC 5024)	13 ^h 12 ^m 55 ^s	+18°09′59″	17.9	n5024b	182	2019 Mar 10	1.0	1.6	5 × 1200
						2019 Mar 11	1.0	0.9	1×404
M15 (NGC 7078)	$21^{h}29^{m}49^{s}$	+12°10′20″	10.4	707811	175	2017 Sep 15	1.1	0.6	13×1200
M2 (NGC 7089)	$21^{h}33^{m}15^{s}$	-00°48′36″	11.5	708911	157	2017 Oct 3	1.1	•••	$3 \times 1200, 1 \times 1800$
				dS	phs				
Sculptor	00 ^h 59 ^m 57 ^s	-33°41′45″	86	bscl5	97	2018 Aug 14	1.8	0.8	3 × 1500
						2018 Sep 10	1.8	0.7	$3 \times 1800, 1 \times 860$
						2018 Sep 11	1.8	0.8	2×1800
Fornax	$02^{h}39^{m}49^{s}$	-34°30′35″	147	bfor7	154	2018 Aug 14	1.8	0.9	$2 \times 1560, 1 \times 1440$
						2018 Sep 10	1.8	0.7	$2 \times 1320, 2 \times 1620$
						2018 Sep 11	2.0	0.8	2×1980
Ursa Major II	$08^{h}52^{m}48^{s}$	+63°05′54″	32	UMaIIb	21	2019 Feb 6	1.5	•••	3×1740
Leo I	$10^{h}08^{m}29^{s}$	+12°18′56″	254	LeoIb	137	2018 Mar 19	1.3	0.8	$2 \times 1620, 1 \times 1560$
						2019 Feb 6	1.1		$2 \times 1860, 1 \times 1920$
						2019 Mar 12	1.2	0.8	$3 \times 1800, 2 \times 1500$
Canes Venatici I	$13^{h}28^{m}03^{s}$	+33°32′44″	218	CVnIa	125	2018 Mar 19	1.1	0.7	$3 \times 1680, 2 \times 1860$
						2018 May 20	1.0	1.0	$1 \times 1200, 2 \times 906$
						2019 Mar 12	1.2	0.8	6 × 1800
Ursa Minor	$15^{h}08^{m}32^{s}$	+67°11′03″	76	bumia	135	2019 Mar 12	1.5	1.4	$4 \times 1800, 2 \times 2100$

2. Observations

Unlike literature catalogs, which generally use high-resolution spectroscropy (HRS) to measure abundances, this work aims to use MRS to measure Mn abundances. MRS was performed using the DEep Imaging Multi-Object Spectrograph (DEIMOS; Faber et al. 2003) on the Keck II telescope. Spectra were obtained for red giant branch (RGB) stars in several globular clusters and classical dSphs. Table 1 lists the observations of the globular clusters and dSphs used in this work.

Our target selection prioritizes globular clusters and dSphs previously observed with the red 1200G grating on DEIMOS. We used a combination of old and newly designed slitmasks. Kirby et al. (2009, 2010, 2016) presented 1200G observations of bscl5, bfor7, n5024b (previously called ng5024), 707811, and 708911. The masks LeoIb, CVnIa, and bumia are very similar to other masks observed by Kirby et al. (2010), but previous observations allowed us to determine membership for some stars. We designed the new masks to have fewer non-members and more confirmed members. We did the same for UMaIIb, where Simon & Geha (2007) observed the previous slitmasks for Ursa Major II.

The previous references describe the membership selection, which we adopt here. In general, members were selected to have radial velocities within $3\sigma_{\nu}$ of the mean velocity. They were also required to have colors and magnitudes consistent with the RGB stars of their respective galaxies.

In this work we used the 1200B grating, which was commissioned in 2017 September. The grating has a groove spacing of 1200 mm⁻¹ and a blaze wavelength of 4500 Å. It provides a dispersion of 0.34 Å pixel⁻¹ for first-order light. The FWHM of the line-spread function is about 1.1 Å. The corresponding resolving power at 5000 Å is $R = \lambda/\Delta\lambda = 4500$. In contrast to DEIMOS's previous complement of gratings, 1200B provides higher resolution than 900ZD and higher throughput at $\lambda < 6000$ Å than 1200G.

We used a central wavelength of 5200 Å, which provided an approximate spectral range of 3900–6500 Å, but the exact spectral range for each slit depended on the location of the slit on the slitmask. The variation in the starting and ending wavelengths was as much as 250 Å. The GG400 order-blocking filter eliminated light bluer than 4000 Å so that second-order light did not contaminate our spectra.

Table 1 details the observations for each field. We observed one slitmask per globular cluster or dwarf galaxy. The coordinates indicate the center of the slitmasks, not necessarily the centers of the stellar systems. The distances are taken from Harris (1996) for globular clusters and McConnachie (2012) for dwarf galaxies. The number of stars represents the total number of slits, including both members and non-members of the corresponding stellar systems. We also report the average airmass and seeing (where available) for the observations.

All observations were reduced using a version of the spec2d pipeline (Cooper et al. 2012; Newman et al. 2013). The pipeline traces the edges of the slits with the help of a spectrally dispersed image of a quartz continuum lamp. The same spectral frame provides for flat-fielding. We used separate exposures of Ne, Ar, Kr, Xe, and Hg arc lamps for wavelength calibration. We identified arc lines with the help of the NIST atomic spectra database (Kramida et al. 2014). After flatfielding and wavelength calibration, the spec2d pipeline performs sky subtraction in 2D and then extracts the spectra into 1D. We modified spec2d in several ways to improve the reliability of the wavelength solution for the 1200B grating. Most notably, we changed one of the subroutines that determined whether an arc line should be included in the wavelength calibration so that usable arc lines were not discarded erroneously.

DEIMOS uses active flexure compensation to keep the data frames aligned within $\sim\!\!0.1$ pixel in both the spatial and spectral directions. The flexure compensation allowed us to stack the 2D images taken within the same week. However, the

compensation becomes unreliable beyond about a week. Over longer timescales, the heliocentric velocity correction varies too much to stack images. Therefore, we reduced images taken within the same week into 1D spectra. For slitmasks observed over multiple weeks, we coadded the 1D spectra after correcting for the change in the heliocentric reference frame.

3. Abundance Measurements

3.1. Description of Pipeline

In this section, we describe the analysis pipeline used to obtain Mn abundances from the reduced and corrected spectra. Broadly speaking, this pipeline fits synthetic spectra with variable Mn abundances to an observed spectrum and uses least-squares fitting to determine the Mn abundance.

3.1.1. Inputs

The main inputs to this pipeline are a line list—a list of atomic and molecular lines in the spectral regions of interest—and estimates of stellar parameters.

To create our line list, we considered 10 Å wide spectral regions around strong Mn lines. Our list of strong Mn lines was initially produced from all Mn absorption lines within the DEIMOS spectral range (≈4500–6500 Å) from the NIST Atomic Spectra Database.⁵ This line list was then vetted by determining which lines were likely to be useful for distinguishing Mn abundances.

First, 10 Å wide spectral regions centered on each Mn line were synthesized and smoothed to match DEIMOS resolution. To determine which Mn lines would be sensitive to a 0.5 dex change in metallicity, we estimated the relative change in line strength for each line:

$$\Delta(f_{\lambda}) = \frac{f_{\lambda}([Mn/H] = 0) - f_{\lambda}([Mn/H] = -0.5)}{f_{\lambda}([Mn/H] = 0)},$$
 (1)

where $f_{\lambda}([Mn/H] = X)$ denotes the flux decrement of the synthetic spectral line at λ assuming a Mn abundance of [Mn/H] = X. Lines were discarded from the list if $\Delta(f_{\lambda})$ was smaller than a threshold value of 1%.

We further determined which Mn lines were likely to be useful by synthesizing spectra using the known Mn abundances of the Sun and of Arcturus and directly comparing each line with the observed spectra of these stars. Any Mn absorption lines for which the amplitudes or shapes of the synthetic spectral lines were strongly inconsistent with the observed spectra were discarded.

Finally, resonance lines (lines with excitation potential 0 eV) were removed from the line list. These lines have been known to yield significantly lower Mn abundances compared to those measured from higher-excitation lines (e.g., Bonifacio et al. 2009; Sneden et al. 2016). Resonance lines are also the most sensitive to deviations from local thermodynamic equilibrium ("non-LTE (NLTE) effects"; e.g., Bergemann & Gehren 2008; Bergemann et al. 2019). We discuss other potential implications of NLTE effects in Section 5.3.

In total we consider 18 Mn lines, described in Table 2. We note that hyperfine structure (HFS) can increase the line strength at fixed abundance, producing Mn abundance corrections of up to \sim 1.5 dex (North et al. 2012). To account for this,

Table 2
Manganese Spectral Lines

4739.1	2.914 2.282 2.953
4754.0	2.953
4761.5	
4762.3	2.889
4765.8	2.941
4766.4	2.920
4783.4	2.300
4823.5	2.320
5399.5	3.850
5407.3	2.143
5420.3	2.143
5516.8	2.178
5537.7	2.187
6013.5	3.072
6016.6	3.075
6021.8	3.075
6384.7	3.772
6491.7	3.763

Table 3Full Line List

Wavelength (Å)	Species ^a	Excitation Potential (eV)	log gf
4729.019	26.0	4.073	-1.614
4729.040	58.1	3.708	-2.780
4729.042	23.0	2.264	-4.909
4729.046	25.1	6.139	-2.998
4729.049	68.0	1.069	-0.037
4729.128	90.0	0.966	-1.221
4729.136	42.0	2.597	-0.785
4729.168	26.0	4.473	-2.658
4729.186	20.0	5.049	-4.150
4729.200	21.0	1.428	-0.530

Note.

^a Atomic species are denoted using the MOOG (Sneden et al. 2012) format of Z.i, where Z is the atomic number of the element and i is its ionization state. (This table is available in its entirety in machine-readable form.)

we used Mn HFS lines from the database maintained by R. L. Kurucz.⁶

Atomic and molecular lines from other species within the $10\,\text{Å}$ wide spectral regions were taken from manually vetted solar absorption line lists from Escala et al. (2019), with oscillator strengths tuned to match HRS of the Sun, Arcturus, and metal-poor globular cluster stars. The full line list used in this work is enumerated in Table 3.

The other required input to the pipeline is a list of stellar parameters. Values for these stellar parameters (effective temperature $T_{\rm eff}$, surface gravity $\log(g)$, Fe-to-H ratio [Fe/H], α -to-Fe ratio [α /Fe], and microturbulent velocity ξ) are adopted from Kirby et al. (2010) for dSph galaxies, and from Kirby et al. (2016) for globular clusters. Microturbulent velocity ξ is calculated from the surface gravity using the empirical formula from Kirby et al. (2009).

The NIST Atomic Spectra Database is available at https://www.nist.gov/pml/atomic-spectra-database.

⁶ The Kurucz line list database is available at http://kurucz.harvard.edu/

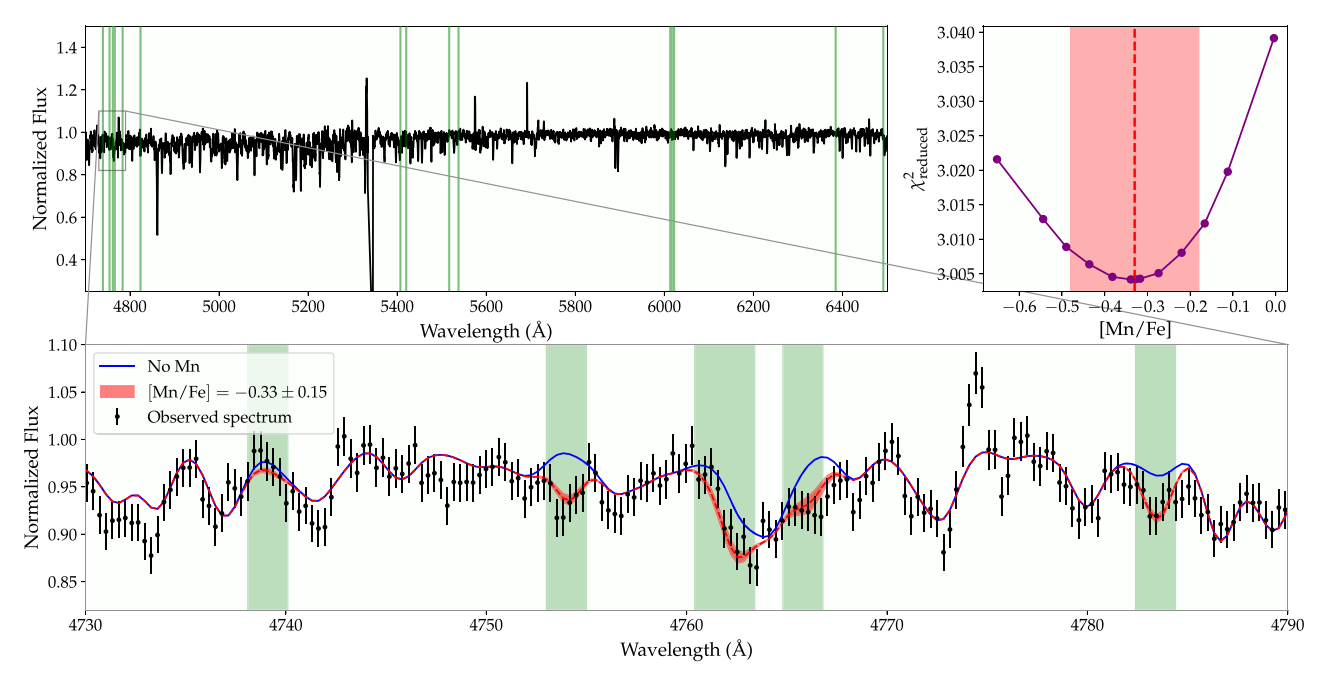


Figure 1. Top left: full continuum-normalized observed spectrum for an example star in Sculptor dSph with a high (>84th percentile in our sample) signal-to-noise ratio S/N = 67. Green shaded regions indicate manganese (Mn) lines. Top right: reduced χ^2 as a function of [Mn/Fe]. The shaded region indicates $\pm 1\sigma$ confidence interval. Bottom: zoomed-in portion of the observed spectrum (black points), again with green shaded vertical bars indicating Mn lines. The median and $\pm \sigma_{\text{stat}}$ best fit are indicated by the red shaded region, while the blue line indicates a fit with negligible [Mn/Fe] ([Mn/H] = -10) for comparison.

3.1.2. Continuum Normalization

Using the input line list and stellar parameters, the automated pipeline can fit synthetic spectra to an observed spectrum. First, the observed spectrum must be corrected for the slowly varying global continuum. To do this, the pipeline synthesizes a spectrum with the same stellar parameters as the observed spectrum, but with a solar Mn abundance. The synthetic spectrum is linearly interpolated from pre-generated spectral grids as in Kirby et al. (2016).

The synthetic spectrum is then interpolated and smoothed using a Gaussian kernel to match the wavelength array and resolution of the observed spectrum. The observed spectrum is divided by the smoothed synthetic spectrum, masking out $\pm 1\,\text{Å}$ regions around Mn lines and other regions with significant continuum fluctuations (e.g., ± 5 pixel regions near the CCD chip gap, $\pm 5\,\text{Å}$ regions around the H α , H β , and H γ Balmer lines, $\pm 8\,\text{Å}$ regions around the strong Na D doublet at $\lambda\lambda 5890$, 5896 Å, and any pixels with negative inverse variances). A cubic spline is fit to the unmasked portions of this quotient with breakpoints every 150 pixels ($\sim\!66\,\text{Å}$). The original observed spectrum is divided by the spline, which represents the global continuum, to obtain the continuum-normalized spectrum.

3.1.3. Spectral Synthesis and Fitting

Synthetic spectra can now be produced and fit to the continuum-normalized observed spectrum. Based on the input stellar parameters, stellar atmosphere models are linearly interpolated from the ATLAS9 grid of one-dimensional plane-parallel stellar atmosphere models (Kurucz 1993). Using these stellar atmosphere models and the line lists described in Section 3.1.1, synthetic spectra with varying Mn abundances are produced using the spectral synthesis code MOOG (Sneden et al. 2012).⁷ To

decrease computation time, only spectral regions $\pm 10\,\text{Å}$ around the Mn lines are synthesized.

As in the continuum normalization process, these synthetic regions are interpolated and smoothed to match the observed spectrum. The pipeline then fits the synthetic regions to the observed spectrum. To determine the best-fitting Mn abundance, a Levenberg-Marquardt least-squares fitting algorithm is used to minimize the χ^2 statistic, with Mn abundance as the free parameter. This is implemented using Python's scipy. optimize.curve_fit function (Jones et al. 2001).

Examples of the best-fit (continuum-normalized) spectra and reduced χ^2 contour are shown for one star in Figure 1. The χ^2 contours of each star were manually inspected, and any stars whose χ^2 contours lacked a clear minimum were removed from analysis. Stars with a fitting error larger than 0.3 dex (a factor of \sim 2) were also removed.

3.2. Uncertainty Analysis

In this section, we first discuss the sources of statistical and systematic uncertainty in our measurements of [Mn/Fe]. We then validate our pipeline and assumed uncertainties by comparing our measurements of [Mn/Fe] with measurements from high-resolution spectroscopy.

3.2.1. Statistical Uncertainty

The statistical uncertainty is dominated by the spectral noise. This manifests in our [Mn/Fe] measurements when fitting synthetic spectra to the observed spectra, since the least-squares statistic is weighted by the uncertainties in the spectra. The statistical uncertainty $\sigma_{\rm stat}$ is therefore given by the square root of the diagonal values of the covariance matrix, which is generated by the <code>scipy.optimize.curve_fit</code> function. The average statistical uncertainty in our [Mn/Fe] measurements is $\langle \sigma_{\rm stat} \rangle = 0.17$ dex.

⁷ We use the 2017 publicly available version of the code, modified as in Sobeck et al. (2011) to properly account for scattering in blue, metal-poor stars.

 Table 4

 Effect of Varying Atmospheric Parameters on [Mn/Fe] Measurements

Object	ID	$\delta [{ m Mn/Fe}]$						
		$T_{\rm eff} \pm 125 { m K}$	$T_{\rm eff}\pm250$ K	$\log g \pm 0.3 \mathrm{dex}$	$\log g \pm 0.6 \mathrm{dex}$			
Scl	1003702	0.02	0.04	0.02	0.05			
Scl	1007989	0.01	0.03	0.01	0.01			
Scl	1009387	0.00	0.01	0.02	0.03			
Scl	1009510	0.01	0.03	0.02	0.02			
Scl	1011529	0.02	0.04	0.04	0.05			
Scl	1014514	0.02	0.03	0.02	0.03			
Scl	1004020	0.02	0.04	0.02	0.02			
Scl	1004084	0.03	0.05	0.01	0.01			
Scl	1004448	0.01	0.04	0.04	0.07			
Scl	1004645	0.03	0.04	0.01	0.02			

(This table is available in its entirety in machine-readable form.)

3.2.2. Systematic Uncertainty

There are several potential sources of systematic uncertainty in our measurement pipeline. Uncertainties in the input stellar parameters, as well as our choice of line list, atmosphere models, and spectral synthesis code can all produce systematic errors in our [Mn/Fe] measurements. We consider some of these sources here.

Atmospheric parameter uncertainties. As described in Section 3.1.1, our [Mn/Fe] measurements require inputs of stellar parameters $T_{\rm eff}$, log g, ξ , [Fe/H], and [α /Fe] in order to synthesize spectra. We assumed fixed values of these parameters, but variations in the atmospheric parameters ($T_{\rm eff}$, log g, ξ) may affect abundance measurements ([Fe/H], [α /Fe], [Mn/Fe]).

We can estimate the effect of varying atmospheric parameters on our [Mn/Fe] measurement. Since the [Mn/Fe] measurement pipeline also requires an input value of [Fe/H], we must first consider how errors in atmospheric parameters ($T_{\rm eff}$, log g) may affect [Fe/H]. We note that we do not consider the effect of varying atmospheric parameters on [α /Fe]. To some extent, measurements of [α /H], [Mn/H], and [Fe/H] will be similarly affected by variations in the atmospheric parameters. We therefore expect that uncertainties in atmospheric parameters will contribute less significantly to errors in abundance ratios like [α /Fe] and [Mn/Fe] than to errors in [Fe/H].

For all stars in our sample, Kirby et al. (2010) estimated the effect of varying $T_{\rm eff}$ and $\log g$ on [Fe/H]. Using these estimates, we can directly quantify systematic errors due to uncertainties in atmospheric parameters: we change $T_{\rm eff}$ by ± 125 and ± 250 K, apply the resulting changes to [Fe/H] (Table 6 of Kirby et al. 2010), then run our pipeline and measure the final variation in [Mn/Fe]. We repeat this procedure for $\log g$, changing $\log g$ by ± 0.3 and ± 0.6 dex. When varying $\log g$, we also vary microturbulent velocity ξ using the calibration derived by Kirby et al. (2009):

$$\xi \text{ (km s}^{-1}) = 2.13 - 0.23 \log g.$$
 (2)

We report the response of [Mn/Fe] to changes in atmospheric parameters for a representative subsample of stars in Sculptor dSph, shown in Table 4. The values listed in this table are the average absolute values of the changes in [Mn/Fe] caused by varying $T_{\rm eff}$ or log g.

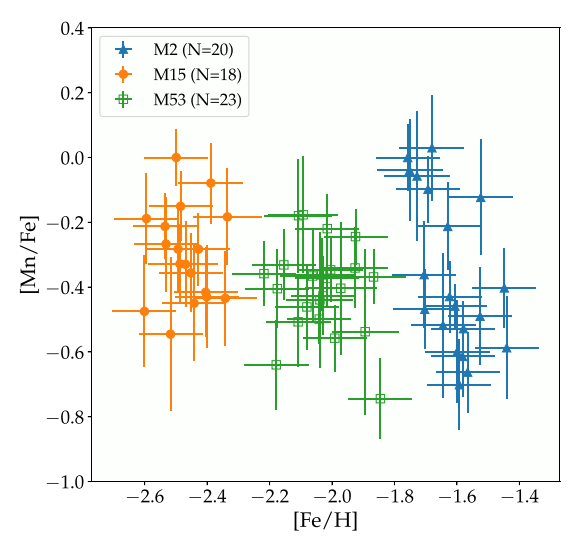
The responses of [Mn/Fe] to variations in atmospheric parameters are approximately linear within $T_{\rm eff} \pm 250$ K and log $g \pm 0.6$ dex. On average, [Mn/Fe] changes by ± 0.014 dex per ± 100 K change in $T_{\rm eff}$. Similarly, [Mn/Fe] changes by ± 0.008 dex per ± 1 dex change in log g. These responses are relatively small compared to the average statistical error ($\langle \sigma_{\rm stat} \rangle = 0.17$ dex), suggesting that any systematic errors in our [Mn/Fe] measurements due to errors in stellar parameters are negligible. As expected, varying $T_{\rm eff}$ and log g affects [Mn/Fe] significantly less than [Fe/H]; Kirby et al. (2010) found [Fe/H] changed by ± 0.092 dex per ± 100 K change in $T_{\rm eff}$ and ± 0.039 dex per ± 1 dex change in log g.

Error floor estimation using globular clusters. Uncertainty in stellar parameters is unlikely to be the only source of systematic uncertainty. However, quantifying all individual sources of the systematic error budget is beyond the scope of this paper. We instead estimate the value of a total systematic error $\sigma_{\rm sys}$ by assuming globular clusters have no intrinsic dispersion in [Mn/Fe]. This $\sigma_{\rm sys}$ subsumes the error from atmospheric parameter variation discussed above, and can be added as an "error floor" to the statistical uncertainties to estimate final uncertainties.

To compute $\sigma_{\rm sys}$, we assume that globular clusters have little intrinsic dispersion in [Mn/Fe]. This assumption does not hold for all stellar abundances; for example, M2 (NGC 7089) appears to host two populations of stars with distinct C, N, Ba, and Sr abundances, suggesting that M2 has a complex SFH (e.g., Lardo et al. 2013). Similarly, M15 (NGC 7078) also displays star-to-star variation in heavy elements (e.g., Sneden et al. 1997). However, since Mn is an Fe-peak element and should be formed in the same sites as Fe, we expect each globular cluster to display roughly zero intrinsic dispersion in [Mn/Fe] abundance.

Following the procedure of Kirby et al. (2010) and Duggan et al. (2018), the assumption of no intrinsic dispersion in [Mn/Fe] suggests that our measurements of [Mn/Fe] should be distributed normally about some mean $\langle [Mn/Fe] \rangle$ with standard deviation equal to the combined statistical and systematic

⁸ Some clusters do have abundance spreads in Fe: ω Centauri (e.g., Johnson & Pilachowski 2010), M54 (Carretta et al. 2010), and Terzan 5 (e.g., Massari et al. 2014). However, these unusual cases are not in our sample.



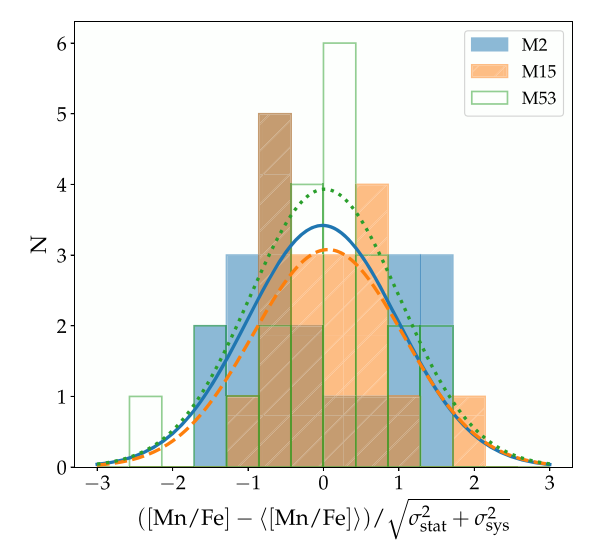


Figure 2. Left: globular cluster [Mn/Fe] abundances measured from medium-resolution spectra as a function of total metallicity [Fe/H]. Right: distribution of deviation from the mean [Mn/Fe], in units of "total error" (including both statistical and systematic error). Lines indicate best-fit normal distributions $\mathcal{N}(0, 1)$.

errors:

stddev
$$\left(\frac{[Mn/Fe] - \langle [Mn/Fe] \rangle}{\sqrt{\sigma_{\text{stat}}^2 + \sigma_{\text{sys}}^2}}\right) = 1.$$
 (3)

The value of $\sigma_{\rm sys}$ can then be computed from Equation (3). This calculation yields $\sigma_{\rm sys}=0.19,\,0.14,\,0.05$ dex for M2, M15, and M53 respectively. To visualize this, the left panel of Figure 2 displays the measured [Mn/Fe] abundances for these globular clusters. The right panel of Figure 2 shows distributions of deviation from the average [Mn/Fe] (i.e., [Mn/Fe] $-\langle {\rm [Mn/Fe]} \rangle)$ in units of the total error $\sqrt{\sigma_{\rm stat}^2+\sigma_{\rm sys}^2}$ for each cluster. The distributions for M15 and M53 are well-fit by a Gaussian with a standard deviation $\sigma=1,$ as expected. M2, on the other hand, appears to have a bimodal distribution of [Mn/Fe]. This may be a result of poor membership selection; M2 has a low radial velocity $|\nu_r|\lesssim 5~{\rm km~s^{-1}};~{\rm e.g.},~{\rm Baumgardt}~{\rm \& Hilker}~2018),$ so velocity selection criteria may have falsely included foreground stars as cluster members.

Based on the intrinsic dispersions of [Mn/Fe] within globular clusters M15 and M53, we estimate an average total systematic [Mn/Fe] error of $\sigma_{\rm sys}=0.10$ dex. This total systematic error is comparable with the statistical error from fitting ($\langle \sigma_{\rm stat} \rangle \sim 0.17$ dex on average). The systematic error and statistical error are added in quadrature to obtain the total error. We use the total [Mn/Fe] errors for the remainder of our analysis.

We note that one of the most significant systematic assumptions in our analysis pipeline is the assumption of LTE. Estimating NLTE corrections for each of the stars in our sample is beyond the scope of this work, particularly since such corrections depend on both $T_{\rm eff}$ and [Mn/Fe], and are different for each Mn line. We instead estimate the overall effect of NLTE corrections on our results by applying a statistical correction, which we discuss later in Section 5.3.

3.2.3. Validation with High-resolution Spectroscopy Comparison

We now validate our pipeline by comparing our [Mn/Fe] measurements, which are derived from MRS, with measurements from HRS. From the literature, we find N = 12 stars in

Table 5
Literature High-resolution Spectroscopy Catalogs

Reference	Object N Atmo		Atmospheres ^a	Code ^b
	Globul	ar clu	sters	
Yong et al. (2014)	M2	2	ATLAS9	MOOG
Sobeck et al. (2006)	M15	2	ATLAS9	MOOG
	d	Sphs		
North et al. (2012)	Sculptor, Fornax	5	MARCS	MOOG, CALRAI
Shetrone et al. (2003)	Fornax, Leo I	2	MARCS	MOOG
Frebel et al. (2010)	Ursa Major II	1	ATLAS9	MOOG

Notes. In all literature catalogs listed here, $T_{\rm eff}$ was measured by requiring Fe I excitation equilibrium, $\log g$ was measured by requiring Fe I and Fe II ionization balance, and ξ was measured by removing abundance trends as a function of equivalent width.

^a ATLAS9: Castelli & Kurucz (2003), http://kurucz.harvard.edu/grids.html; MARCS: Gustafsson et al. (1975, 2003, 2008), http://marcs.astro.uu.ee

b MOOG: Sneden et al. (2012); CALRAI: Spite (1967). North et al. (2012) used CALRAI for initial abundance measurements and MOOG for HFS corrections.

our sample that have HRS measurements; this small sample size is largely due to Mn's weak lines in the blue part of the optical wavelength range, which make it difficult to measure Mn from HRS. In Table 5, we list the literature catalogs that contain HRS measurements for these 12 stars. In Table 6, we list the MRS and HRS measurements of [Mn/Fe] for these stars, as well as the stellar parameters used in the HRS measurements.

The left panel of Figure 3 compares our medium-resolution measurements ([Mn/Fe]_{MRS}) with the literature HRS measurements ([Mn/Fe]_{HRS}). The difference between these measurements ([Mn/Fe]_{MRS} – [Mn/Fe]_{HRS}) is on average -0.03 dex. This is significantly smaller than the median MRS and HRS errors reported for this comparison sample ($\sigma_{median,MRS} \sim 0.10$ dex

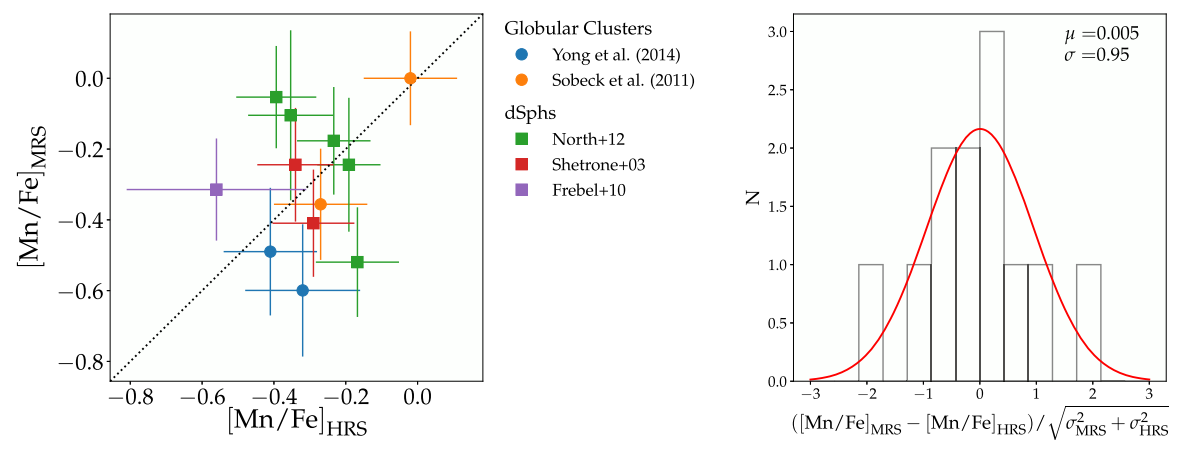


Figure 3. Left: comparison between our [Mn/Fe] measurements from medium-resolution spectra $([Mn/Fe]_{MRS})$ and literature measurements from high-resolution spectra $([Mn/Fe]_{HRS})$. The dotted line denotes the 1:1 line; circles (squares) denote stars from globular clusters (dSphs). Right: histogram of the differences between medium-resolution and high-resolution [Mn/Fe] measurements. The red line denotes the best-fit Gaussian distribution.

 Table 6

 Comparison between DEIMOS Abundances and Literature High-resolution Abundances

Object ID	Reference		MRS					
			T _{eff} (K)	$\log g$ (cm s ⁻²)	(km s^{-1})	[Fe/H] (dex)	[Mn/Fe] ^b (dex)	[Mn/Fe] (dex)
M2	An08-A1045	Yong et al. (2014)	4275	0.70	1.78	-1.66	-0.41 ± 0.13	-0.49 ± 0.18
M2	An08-A13934	Yong et al. (2014)	4325	1.30	1.88	-0.97	-0.32 ± 0.16	-0.60 ± 0.19
M15	33889	Sobeck et al. (2006)	4350	0.60	1.65	-2.59	-0.06 ± 0.13	$+0.00 \pm 0.13$
M15	41376	Sobeck et al. (2006)	4225	0.30	1.85	-2.44	-0.31 ± 0.13	-0.36 ± 0.16
Scl	1008833	North et al. (2012)					-0.27 ± 0.10	-0.18 ± 0.15
Scl	1005457	North et al. (2012)					-0.21 ± 0.12	-0.52 ± 0.15
For	37141	North et al. (2012)					-0.43 ± 0.11	-0.05 ± 0.14
For	54557 ^c	North et al. (2012)					-0.23 ± 0.09	-0.24 ± 0.19
For	67094	North et al. (2012)					-0.39 ± 0.12	-0.10 ± 0.24
For	54557 ^c	Shetrone et al. (2003)	4025	0.00	2.00	-1.21	-0.40 ± 0.11	-0.24 ± 0.19
LeoI	S60286	Shetrone et al. (2003)	4250	0.80	2.20	-1.52	-0.35 ± 0.11	-0.41 ± 0.18
UMaII	176_103	Frebel et al. (2010)	4550	1.00	2.20	-2.34	-0.56 ± 0.25	-0.31 ± 0.17

Notes.

and $\sigma_{\rm median,HRS}\sim0.16$ dex, respectively), suggesting that the MRS and HRS measurements are largely consistent. However, there is no clear correlation between the MRS and HRS measurements, likely because our comparison sample is small and covers only a narrow range of [Mn/Fe].

Assuming that both MRS and HRS measurements have accurately estimated the total (including statistical and systematic) errors, the differences between them ([Mn/Fe]_{MRS} – [Mn/Fe]_{HRS}) should be distributed normally about mean zero with standard deviation equal to the combined MRS and HRS errors ($\sqrt{\sigma_{HRS}^2 + \sigma_{MRS}^2}$).

To check this, we plot a histogram of the differences between MRS and HRS measurements in the right panel of Figure 3. The best-fit Gaussian distribution to this histogram (red line) has a mean of 0.005 dex and a standard deviation 0.95 dex, similar to the expected normal distribution $\mathcal{N}(0, 1)$.

This suggests that the total errors in our [Mn/Fe] measurements are consistent with HRS errors.

We note that many of the HRS measurements use resonance lines, which are particularly sensitive to NLTE effects (Bergemann et al. 2019); as discussed in Section 3.1.1, we remove resonance Mn lines from our line list for that reason. This may also contribute to systematic offsets between our MRS measurements and HRS literature measurements. Furthermore, the HRS measurements are not a flawless comparison set; the HRS catalogs use heterogeneous measurement techniques, which may introduce additional systematic offsets among catalogs.

3.3. Mn Abundance Catalog

Finally, we present all Mn abundances measured from MRS in Table 7. We list here the stellar parameters $T_{\rm eff}$, $\log(g)$,

^a Sobeck et al. (2006) obtained stellar parameters from Sneden et al. (1997). The stellar parameters used by North et al. (2012) are not publicly available.

^b The errors on HRS [Mn/Fe] measurements were computed differently in each of the literature sources. However, for the most part all HRS catalogs have accounted for both statistical error (i.e., uncertainty from different Mn lines) as well as systematic error (including uncertainty from stellar parameters) in their error estimates. The only exception is the North et al. (2012) HRS catalog, which does not report errors on total [Mn/Fe] abundances. For the North et al. (2012) abundances, the errors listed are only the *statistical* errors, estimated as the standard deviation of abundances measured from different Mn lines.

^c The star 54557 has two separate HRS measurements from North et al. (2012) and Shetrone et al. (2003). We list them as separate entries for completeness.

 Table 7

 Manganese Abundance Catalog of GC and dSph Stars

Object	ID	T _{eff} (K)	$\log g \atop (\text{cm s}^{-2})$	ξ (km s ⁻¹)	$\begin{array}{c} [\alpha/\text{Fe}] \\ (\text{dex}) \end{array}$	[Fe/H] (dex)	[Mn/Fe] ^a (dex)
			Gl	lobular Clusters			
M15 M15 M15 M15 M15	15681 31227 33889 36569 37854	5275 ± 35 4470 ± 19 4820 ± 25 4409 ± 20 4963 ± 48	$+3.02 \pm 0.10$ $+1.06 \pm 0.10$ $+1.72 \pm 0.10$ $+0.86 \pm 0.10$ $+2.09 \pm 0.10$	1.43 ± 0.10 1.89 ± 0.06 1.73 ± 0.07 1.94 ± 0.06 1.65 ± 0.08	$+0.18 \pm 0.10$ $+0.23 \pm 0.09$ $+0.44 \pm 0.09$ $+0.22 \pm 0.09$ $+0.50 \pm 0.10$	-2.39 ± 0.10 -2.49 ± 0.10 -2.50 ± 0.10 -2.52 ± 0.10 -2.59 ± 0.10	-0.08 ± 0.16 -0.33 ± 0.16 $+0.00 \pm 0.13$ -0.55 ± 0.26 -0.19 ± 0.17
				dSphs			
Scl Scl Scl Scl Scl	1003702 1007989 1009387 1009510 1011529	4660 ± 54 4849 ± 92 4597 ± 101 4677 ± 57 4510 ± 54	$+1.58 \pm 0.10$ $+2.12 \pm 0.10$ $+1.53 \pm 0.10$ $+1.76 \pm 0.10$ $+1.29 \pm 0.10$	$\begin{array}{c} 1.77 \pm 0.07 \\ 1.64 \pm 0.08 \\ 1.65 \pm 0.08 \\ 1.81 \pm 0.07 \\ 1.72 \pm 0.07 \end{array}$	$+0.31 \pm 0.14$ $+0.22 \pm 0.31$ $+0.01 \pm 0.25$ $+0.20 \pm 0.13$ -0.02 ± 0.15	-1.95 ± 0.11 -1.42 ± 0.13 -1.50 ± 0.21 -1.80 ± 0.11 -1.48 ± 0.11	$-0.52 \pm 0.22 -0.23 \pm 0.22 -0.43 \pm 0.21 -0.31 \pm 0.21 -0.41 \pm 0.15$

Note.

(This table is available in its entirety in machine-readable form.)

[Fe/H], [α /Fe], and ξ (from Kirby et al. 2010) used as inputs in the pipeline to measure [Mn/Fe], as well as the total error in [Mn/Fe] ($\sigma = \sqrt{\sigma_{\rm sys}^2 + \sigma_{\rm stat}^2}$).

The full catalog contains Mn abundance measurements of 61 stars from three globular clusters and 161 stars from six dSph galaxies. This is one of the largest self-consistent samples of dwarf galaxy Mn abundances measured to date. As previously noted, high-resolution measurements are often heterogenous in their assumptions (e.g., Table 6). The internal consistency of this catalog makes it particularly useful for galactic archaeology studies that require statistical samples of abundances. In the next sections, we use our sample of [Mn/Fe] abundances in dSphs for such a study.

4. Mn Yields in Sculptor

4.1. Inferring [Mn/Fe] Yields from a Simple Chemical Evolution Model

With our measured Mn abundances, we can now estimate how much of this Mn is produced by SNe Ia. Following the procedure of Kirby et al. (2019), we determined SN Ia yields of Mn by assuming a simple chemical evolution model. We refer readers to Kirby et al. (2019) for a more detailed discussion of this model, but summarize this procedure briefly here.

This simple model assumes that CCSNe are the only nucleosynthetic sources at early times, and that CCSN yields are independent of total metallicity ([Fe/H]). The stars formed at such early times will have low [Fe/H]; furthermore, these stars will all have the same chemical abundances determined by the CCSN yields. Put another way, for any element X, [X/Fe] will be constant as a function of [Fe/H] for low-[Fe/H] stars.

After some delay time, SNe Ia will begin to explode and produce different yields of element X. Therefore, for stars with metallicities above some threshold $[Fe/H]_{Ia}$, [X/Fe] will begin to deviate from the original CCSN-only value $([X/Fe]_{CC})$. We

can model this behavior with the following parameterization:

$$[X/Fe] = \begin{cases} [X/Fe]_{CC} & [Fe/H] \leqslant [Fe/H]_{Ia} \\ [Fe/H] \tan \theta + \frac{b_{\perp}}{\cos \theta} & [Fe/H] > [Fe/H]_{Ia} \end{cases}$$
(4)

where continuity is enforced at $[Fe/H] = [Fe/H]_{Ia}$. As described in Kirby et al. (2019), the sloped line in the $[Fe/H] > [Fe/H]_{Ia}$ regime is parameterized by an angle (θ) and perpendicular offset (b_{\perp}) rather than by a slope and intercept, in order to avoid biasing the linear fit toward shallower slopes (Hogg et al. 2010).

Using this model, the free parameters $[Fe/H]_{Ia}$, b_{\perp} , and θ can be determined by maximizing the likelihood function L (Equations (3)–(6) in Kirby et al. 2019). To do the fitting, we used the emcee Python module (Foreman-Mackey et al. 2013) to minimize $-\ln L$ by implementing a Markov chain Monte Carlo (MCMC) ensemble sampler. We ran 100 ensemble members or "walkers," each with 10^5 links sampled using a Metropolis–Hastings algorithm. We discarded the first 10^4 "burn-in" links.

We assumed uniform priors on b_{\perp} and θ , but we used the values of $[Fe/H]_{Ia}$ previously measured by Kirby et al. (2019). As in Kirby et al., we imposed an additional prior to avoid negative values of the linear ratio $(Mn/Fe)_{Ia}$, which are unphysical: if any step in the MCMC chain yields $(Mn/Fe)_{Ia} < 0$, we set the likelihood equal to zero. We further imposed a prior on $[Mn/Fe]_{CC}$:

$$P = \frac{1}{\sqrt{2\pi\sigma_{\rm Mn}}} \exp\left(-\frac{([\rm Mn/Fe]_{\rm halo} - [\rm Mn/Fe]_{\rm CC})^2}{2\sigma_{\rm Mn}^2}\right). \quad (5)$$

Based on high-resolution measurements of metal-poor stars in the Milky Way halo compiled in the online database JINAbase (Abohalima & Frebel 2018), we set $[Mn/Fe]_{halo} = -0.3$ and

^a The errors reported here are total errors (statistical and systematic errors added in quadrature). The statistical (fitting) errors can be obtained by removing the contribution from the systematic error, which we estimate (see Section 3.2.3) to be $\sigma_{sys} = 0.10$ dex.

⁹ Specifically, we assumed $b_{\perp} \sim \mathcal{U}\{-10, 10\}$ and $\theta \sim \mathcal{U}\left\{-\frac{\pi}{2}, \frac{\pi}{2}\right\}$.

 $^{^{10}}$ Note that Kirby et al. (2019) also imposed an additional prior on $[Mg/Fe]_{CC},$ since Mg is almost entirely produced in CCSNe.

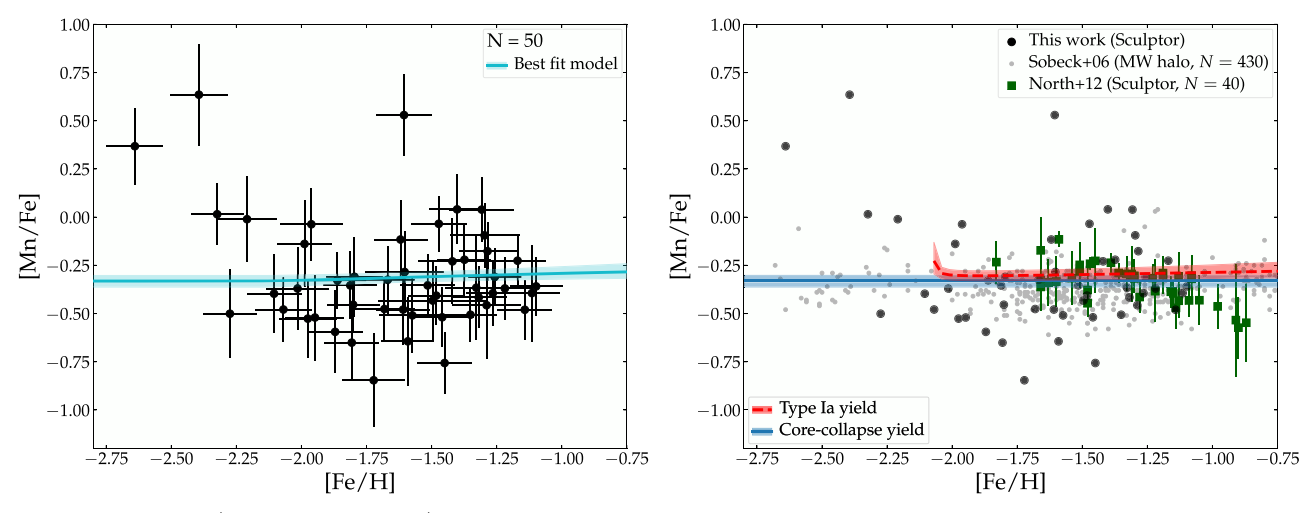


Figure 4. Left: measured [Mn/Fe] as a function of [Fe/H] for Sculptor dSph (black points). The cyan solid line marks the median best-fit model, and the cyan shaded region denotes the 68% confidence interval about the median. Right: the same, but errorbars have been removed from black points for illustration purposes. The red dashed line and shaded region marks the Type Ia [Mn/Fe] yield, and the blue solid line and shaded region marks the CCSN [Mn/Fe] yield computed from the model. Green squares denote measurements for Sculptor dSph from North et al. (2012) (note that error bars only denote statistical rather than total errors); small gray points denote measurements of Milky Way halo globular cluster and field stars from Sobeck et al. (2006).

 $\sigma_{\rm Mn}=0.1$. We found that this additional prior on $({\rm Mn/Fe})_{\rm CC}$ does not significantly affect our results, since the enforced continuity at $[{\rm Fe/H}]_{\rm Ia}$ requires a low inferred value of $({\rm Mn/Fe})_{\rm CC}$.

The MCMC sampled the posterior distribution of the parameters b_{\perp} and θ . The initial values of b_{\perp} and θ were chosen by performing a simple linear fit to the [Mn/Fe] versus [Fe/H] trend for [Fe/H] > [Fe/H]_{Ia}. Unless otherwise noted, for all quantities we report the median (50th percentile) value and 68% confidence intervals about the median.

For Sculptor, we find that [Mn/Fe] is near-constant as a function of [Fe/H], with $\theta=1.61^{+2.45}_{-1.30}$ degrees and $b_{\perp}=-0.26^{+0.07}_{-0.05}$ dex. The data and corresponding best-fit model are shown in the left panel of Figure 4. There are three high-[Mn/Fe] outliers, but removing them does not significantly change our main results, again due to the enforcement of continuity in our model.

Using this best-fit model, we can infer the CCSN and SN Ia yields of Mn from the parameters b_{\perp} and θ . As described in Kirby et al. (2019), the CCSN yield of [Mn/Fe] can be calculated as

$$[Mn/Fe]_{CC} = \frac{b_{\perp}}{\cos \theta} + [Fe/H]_{Ia} \tan \theta.$$
 (6)

The SN Ia yield can then be determined from

$$\left(\frac{\mathrm{Mn}}{\mathrm{Fe}}\right)_{\mathrm{Ia}} = \frac{R+1}{R} \left(\frac{\mathrm{Mn}}{\mathrm{Fe}}\right)_{\star} - \frac{1}{R} \left(\frac{\mathrm{Mn}}{\mathrm{Fe}}\right)_{\mathrm{CC}} \tag{7}$$

where $R \equiv \frac{\mathrm{Fe_{Ia}}}{\mathrm{Fe_{CC}}}$ is the amount of Fe produced by SNe Ia relative to that produced by CCSNe. Note that Equation (7) does not use bracket notation, as it includes linear rather than logarithmic element ratios.

Using these equations, we compute the [Mn/Fe] yields for Sculptor. These are denoted in the right panel of Figure 4 by the blue and red shaded regions, which represent the inferred CCSN and SN Ia yields, respectively. We find [Mn/Fe]_{CC} = $-0.33^{+0.03}_{-0.03}$ for CCSNe, and [Mn/Fe]_{Ia} = $-0.30^{+0.03}_{-0.03}$ at [Fe/H] = -1.5 dex for SNe Ia.

Although we have Mn measurements for stars in the dSphs Ursa Minor, Ursa Major II, Canes Venatici I, Leo I, and Fornax, we do not include them in this section. In Ursa Minor, Ursa Major II, and Canes Venatici I, the samples of stars for which we were able to measure [Mn/Fe] are so small that we cannot draw meaningful conclusions. Leo I and Fornax are not well fit by our simple chemical evolution model. We discuss these other dSphs later in Section 5.2.

4.2. Comparison with Prior Work

We now compare our measurements with previous literature. The right panel of Figure 4 compares the Sculptor dSph Mn abundances from this work (black points) directly with those measured by North et al. (2012) (green squares) and Sobeck et al. (2006) (small gray points).

Our measurements imply that in Sculptor, [Mn/Fe] is roughly constant with respect to [Fe/H], suggesting that the overall Mn abundance does not change with time—and that SNe Ia and CCSNe produce roughly the same yields of Mn with respect to Fe. This is consistent with North et al. (2012), who published the previously largest literature catalog of Mn abundances in Sculptor. North et al. (2012) obtained Mn abundances for $\sim\!\!40$ stars from high-resolution spectroscopy. From their measurements, they found a plateau in [Mn/Fe] at metallicities $-1.75 \lesssim [Fe/H] \lesssim -1.4$, which largely agrees with our finding of metallicity-independent [Mn/Fe].

However, at a given [Fe/H], our measurements indicate a larger spread in [Mn/Fe] than North et al. (2012) find. This may be because of the different line lists used. While we use the same 5407 Å, 5420 Å, and 5516 Å Mn lines that North et al. (2012) use, we use also 15 other lines, including several in the bluer range of the optical spectrum (4700–5000 Å). According to our line sensitivity analysis (Section 3.1.1) these blue lines are among the most sensitive to Mn abundance, so our measurements may be able to probe lower [Mn/Fe] than North et al. (2012), who discard any stars in their sample with "unreliable" Mn lines.

Furthermore, at higher metallicities North et al. (2012) reported a decreasing trend of [Mn/Fe] with respect to [Fe/H]

in Sculptor dSph. This trend does not appear in any of the other galaxies measured in their work, although the authors noted that a similar trend has also been observed for giants and subgiants in the globular cluster ω Centauri (Cunha et al. 2010; Pancino et al. 2011). North et al. (2012) interpreted the decreasing trend as the result of metallicity-dependent Mn yields from SNe Ia. We are unable to confirm this downward trend at higher metallicities, since we do not observe stars with $[Fe/H] \gtrsim -1.1$.

On the other hand, our observed [Mn/Fe]–[Fe/H] relation is remarkably consistent with Mn abundances measured from \sim 200 Milky Way cluster and field halo stars by Sobeck et al. (2006). Sobeck et al. (2006) found an average constant value of $\langle [Mn/Fe] \rangle = -0.36$ for Milky Way halo field stars, which agrees within typical uncertainties with our measured average $\langle [Mn/Fe] \rangle = -0.30$. We note that Feltzing et al. (2007) reported [Mn/Fe] yields for main-sequence and subgiant stars in the Milky Way thick disk that are on average 0.15 dex higher than the Sobeck et al. (2006) measurements at [Fe/H] ~ -1 . As North et al. (2012) suggested, this slight discrepancy may be due to differences in the line lists used, or differences in NLTE corrections between giants and less evolved stars (e.g., Bergemann et al. 2019). At higher metallicities ([Fe/H] $\gtrsim -1$), Feltzing et al. (2007) found that [Mn/Fe] begins to increase to super-solar abundances. This may suggest that the thick disk has a nucleosynthetic history that is distinct from the histories of the Galactic halo and Sculptor dSph. We return to this point in Section 5.2, where we discuss the potential role of SFH in driving [Mn/Fe].

Cescutti & Kobayashi (2017) compiled measurements from $N \sim 20$ stars from other dSphs: Ursa Minor, Sextans, and Carina. They observed a "butterfly"-shaped distribution of [Mn/ Fe] as a function of [Fe/H], i.e., large spreads in [Mn/Fe] at $-3.5 \lesssim [\text{Fe/H}] \lesssim -2.0 \text{ and } -1.75 \lesssim [\text{Fe/H}] \lesssim -1.0, \text{ with a}$ narrow spread at an intermediate metallicity ([Fe/H] ~ -2.0). Cescutti & Kobayashi (2017) suggested that this distribution might be characteristic of a stochastic chemical evolution model with two channels: a sub- $M_{\rm Ch}$ channel and a near- $M_{\rm Ch}$ channel with relatively weak deflagrations (a "Type Iax" SN channel). We do not directly compare their results with ours, since their chemical evolution model was tuned to match the metallicity distribution function of Ursa Minor. However, we do note that the spread in our measurements ($\sigma \sim 0.29$ dex, computed as the standard deviation of all [Mn/Fe] measurements in Sculptor) is roughly consistent with the spreads predicted by these stochastic models, perhaps suggesting that the chemical evolution of Sculptor dSph is also stochastic.

Finally, we briefly discuss nucleosynthetic yields measured from X-ray emission from Type Ia supernova remnants (SNRs). Yamaguchi et al. (2015) compile literature Mn-to-Fe ratios for three Milky Way SNRs. Kepler's SNR, Tycho's SNR, and 3C 397 are measured to have Mn yields of [Mn/Fe] = 0.08 ± 0.17 , 0.22 ± 0.20 , and 0.47 ± 0.14 , respectively. While these super-solar abundances are much higher than our best-fit model ([Mn/Fe]_{Ia} ~ -0.3), these SNRs are also young and likely had progenitors with near-solar metallicities, so they are not directly comparable with our measurements. Their super-solar abundances may be more consistent with other measurements of high-metallicity Galactic thick disk stars (Feltzing et al. 2007).

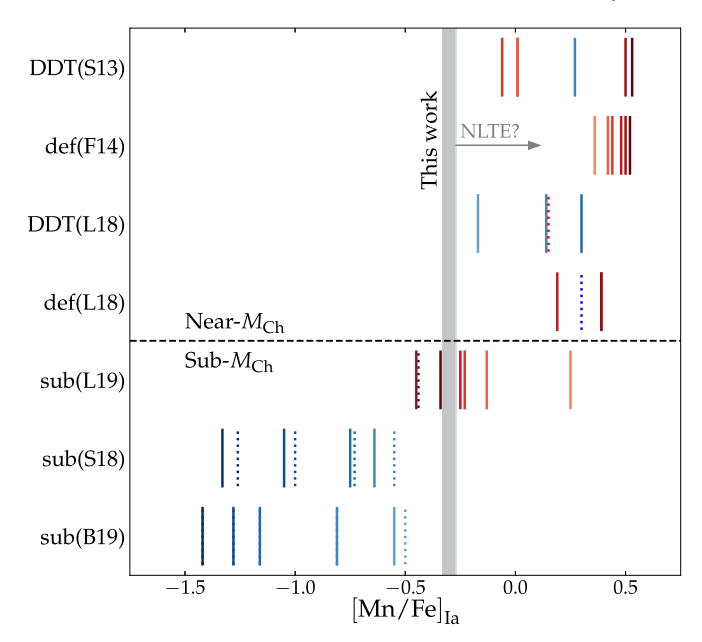


Figure 5. SN Ia [Mn/Fe] yield (at [Fe/H] = -1.5) measured in Sculptor dSph from this work (gray shaded region, marking $\pm 68\%$ confidence interval about the median), compared to theoretical yields from various models (vertical lines). Models are described in more detail in the Appendix. The dashed horizontal line separates near- $M_{\rm Ch}$ (above line) and sub- $M_{\rm Ch}$ (below line) models. Red (blue) lines indicate theoretical yields from solar metallicity ($10^{-1.5}Z_{\odot}$) progenitors. Darker shading indicates more ignition sites (S13 and F14), higher initial density (L18), or higher-mass WD progenitors (L19, S18, and B19). Dotted lines indicate special cases, denoted with asterisks in Tables 9 and 10. The gray arrow shows the maximal effect of applying NLTE corrections to our result (Section 5.3). See Table 8 for these references in full.

5. Implications for SN Ia Physics

We now consider the implications of our measurements on SN Ia physics. We compare our observationally inferred SN Ia yield for Sculptor with yields predicted from theoretical models (Section 5.1) before discussing the interpretation of [Mn/Fe] abundances in other dSph galaxies (Section 5.2). Finally, we consider our assumption of LTE and its impact on our results (Section 5.3).

5.1. Comparison with Theoretical Models

Figure 5 compares our inferred SN Ia yield from Sculptor dSph with yields predicted from various theoretical simulations. We discuss these models and their predicted [Mn/Fe] yields in further detail in the Appendix. We list the most relevant model details in Table 8, reproduced from Table 2 of Kirby et al. (2019).

As discussed in Section 1.2, $[Mn/Fe]_{Ia}$ places a strong constraint on the mass of an SN Ia progenitor. This is shown in Figure 5; nearly all of the near- M_{Ch} models (above the horizontal dashed line) produce solar or super-solar $[Mn/Fe]_{Ia}$, while the sub- M_{Ch} models can produce significantly sub-solar $[Mn/Fe]_{Ia}$. We note that, when possible, we consider near- M_{Ch} models with $\sim 1/3Z_{\odot}$ to account for core convective burning in these progenitors; we describe this "simmering" process further in the Appendix. We also note that the pure deflagration models def(F14) and def(L18) may represent near- M_{Ch} SNe Iax. Of the near- M_{Ch} models, our measured $[Mn/Fe]_{Ia}$ is most consistent with the low-density DDT model by L18, which is

Table 8 SN Ia Models

Model	Reference	Description
DDT(S13)	Seitenzahl et al. (2013b)	$M_{\rm Ch}$, 3D, DDT, multiple ignition sites
def(F14)	Fink et al. (2014)	$M_{\rm Ch}$, 3D, pure deflagration, multiple ignition sites
DDT(L18)	Leung & Nomoto (2018)	$M_{\rm Ch}$, 2D, DDT, varying initial central density
def(L18)	Leung & Nomoto (2018)	$M_{\rm Ch}$, 2D, pure deflagration, varying initial central density
sub(L19)	Leung & Nomoto (2020)	sub- $M_{\rm Ch}$, 2D, double detonation with He shell
sub(\$18)	Shen et al. (2018b)	sub- $M_{\rm Ch}$, 1D, detonation of bare CO WD, two choices of C/O mass ratio
sub(B19)	Bravo et al. (2019)	sub- M_{Ch} , 1D, detonation of bare CO WD, two choices of $^{12}\mathrm{C}$ + $^{16}\mathrm{O}$ reaction rate

Note. Reproduced from Table 2 of Kirby et al. (2019).

the only near- $M_{\rm Ch}$ model to have a sub-solar [Mn/Fe] yield. ¹¹ This model has a low central density of 1×10^9 g cm⁻², producing a larger detonation region which produces a very low [Mn/Fe] yield at low metallicity. However, this central density may be unphysically low for single-degenerate SNe Ia (e.g., Figure 4 in Lesaffre et al. 2006).

Of the sub- M_{Ch} models, our measured SN Ia yield of $[Mn/Fe]_{Ia} = -0.30^{+0.03}_{-0.03}$ is most consistent with L19's solar metallicity models between 1.05 and 1.20 M_{\odot} . However, this is not a straightforward comparison, since we measure $[Mn/Fe]_{Ia}$ at [Fe/H] = -1.5 rather than at solar metallicity. Of the remaining models, our measured [Mn/Fe]Ia is most consistent with the sub-M_{Ch} models of S18 and B19, requiring WD masses $< 0.9 M_{\odot}$. This mass constraint is lower than estimated by Kirby et al. (2019), who found that their measured yields of Ni matched SN Ia models from ~ 1.00 to $1.15 M_{\odot}$. This discrepancy may simply be due to uncertainties in the theoretical yields; as Figure 5 shows, different sub- $M_{\rm Ch}$ models produce a wide range of [Mn/Fe]Ia yields due to varying physical assumptions made in the models. Alternatively, our observationally inferred yield may be incorrect. The largest uncertainty in our measurement is the assumption of LTE, and we address the effect of NLTE corrections in Section 5.3.

If we take the theoretical yields and our observationally inferred yield at face value, then the difference between SN Ia models best fit by $[Mn/Fe]_{Ia}$ and $[Ni/Fe]_{Ia}$ yields must have a physical explanation. Perhaps the most plausible explanation is that our measured yield is a combination of yields from both sub- M_{Ch} and near- M_{Ch} SNe Ia or SNe Iax.

We further explore this hypothesis by considering the metallicity dependence of our measured [Mn/Fe]_{Ia}. In Figure 6, we plot [Mn/Fe]_{Ia} as a function of [Fe/H] and compare against theoretical predictions. Our observationally inferred [Mn/Fe]_{Ia} is near-constant as a function of metallicity across the range $-2 \lesssim$ [Fe/H] $\lesssim -1$. However, the theoretical sub- $M_{\rm Ch}$ models generally predict much larger increases in [Mn/Fe]_{Ia} with metallicity. This discrepancy may indicate that the combination of sub- $M_{\rm Ch}$ and near- $M_{\rm Ch}$ SNe Ia depends on metallicity. ¹²

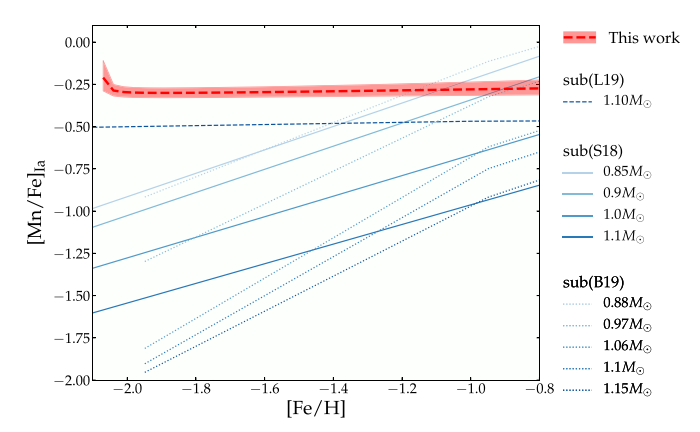


Figure 6. SN Ia yield of Mn [Mn/Fe]_{Ia} as a function of [Fe/H]. The red dashed line and shaded region represent our inferred yield from Sculptor dSph, as shown in Figure 4. Other lines denote yields from various sub- $M_{\rm Ch}$ theoretical models.

We can roughly estimate the fractions of sub- $M_{\rm Ch}$ and near- $M_{\rm Ch}$ SNe Ia required to produce our inferred [Mn/Fe]_{Ia}. For example, at low [Fe/H], we infer a higher [Mn/Fe]_{Ia} than sub- $M_{\rm Ch}$ SNe—particularly low-metallicity sub- $M_{\rm Ch}$ SNe—can produce. As a conservative estimate, we consider the low-metallicity sub- $M_{\rm Ch}$ model that is least discrepant with our observed [Mn/Fe]_{Ia}: the L19 1.1 M_{\odot} model. At [Fe/H] ~ -2 , this model has a yield of [Mn/Fe]_{Ia} ~ -0.50 , nearly ~ 0.25 dex lower than our best-fit model. Therefore, assuming an average near- $M_{\rm Ch}$ yield from the S13 N100 model, at least $\sim 20\%$ of SNe must be near- $M_{\rm Ch}$ SNe to reproduce our best-fit model.

If we instead compare our observationally inferred yield with a more strongly metallicity-dependent model like those of S18, we can estimate the fraction of near- $M_{\rm Ch}$ SNe Ia or SNe Iax over a range of metallicities. Assuming $\sim 1\,M_{\odot}$ WD progenitors as predicted by Kirby et al. (2019), we find that using S18's models, $\sim 33\%$ of SNe Ia at [Fe/H] ~ -1 and $\sim 36\%$ of SNe Ia at [Fe/H] ~ -2 must be near- $M_{\rm Ch}$. These estimates are somewhat higher than the fractions inferred from Kirby et al.'s (2019) [Ni/Fe] measurements; using the S18 1 M_{\odot} model yields for [Ni/Fe], only $\sim 22\%$ of SNe Ia must be near- $M_{\rm Ch}$.

We emphasize that these fractions are only rough estimates, subject to uncertainties in both the observational and theoretical yields. However, our data suggest that some non-negligible fraction of SNe Ia must have near- $M_{\rm Ch}$ progenitors over the metallicity range $-2 \lesssim [{\rm Fe/H}] \lesssim -1$. Furthermore, the near- $M_{\rm Ch}$ fraction does not appear to change significantly across the metallicity range probed by our observations. This may change at higher metallicities ([Fe/H] $\gtrsim -1$), where near- $M_{\rm Ch}$ SNe Ia may begin to dominate, producing super-solar

 $[\]overline{11}$ The gravitationally confined detonation of a near- $M_{\rm Ch}$ WD may also have a similar sub-solar [Mn/Fe] yield; for example, Seitenzahl et al. (2016) find [Mn/Fe] = -0.13 for one such model. However, the other observables (particularly spectral features of other IMEs) predicted by this model do not match typical SNe Ia, and this model is therefore not expected to be a dominant channel of SNe Ia.

¹² This discrepancy may also be exacerbated by the dependence of [Mn/Fe] yields on the mass of sub- $M_{\rm Ch}$ SNe Ia. More massive sub- $M_{\rm Ch}$ WDs produce lower [Mn/Fe] yields, and younger stellar populations should preferentially host these more massive sub- $M_{\rm Ch}$ WD explosions. We therefore expect [Mn/Fe]_{Ia} to be even lower at low [Fe/H].

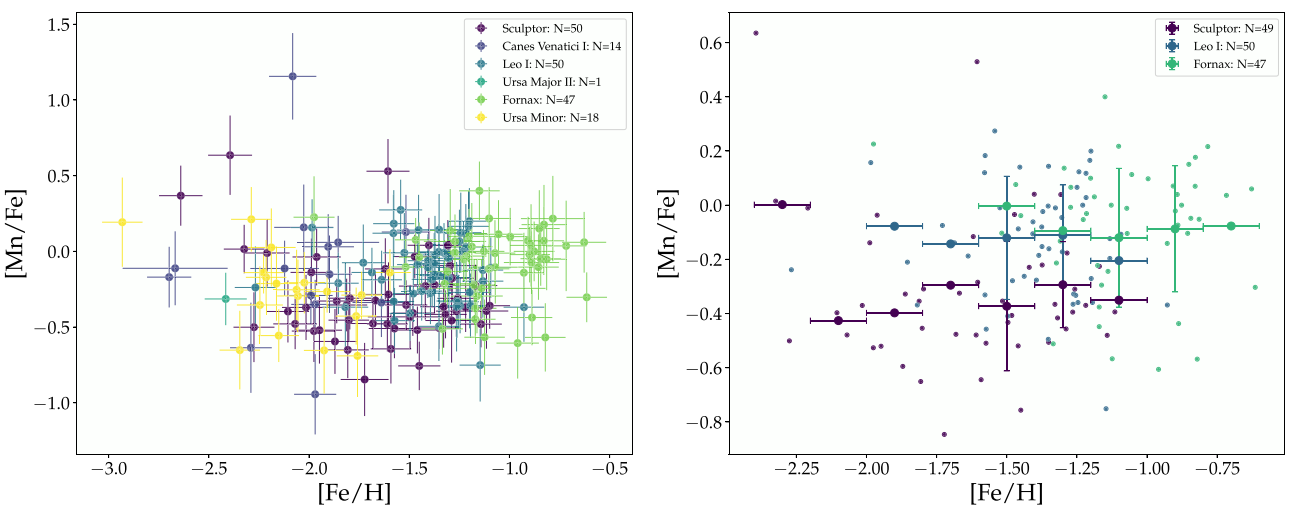


Figure 7. Left: [Mn/Fe] as a function of [Fe/H] for all dSph galaxies in our sample. Right: the same, but zoomed in to show only stars from Sculptor, Leo I, and Fornax dSphs. Small points denote the measured abundances (errorbars have been removed for ease of visualization), and large points with errorbars denote the weighted averages in each 0.2 dex metallicity bin (only bins with >1 stars are plotted, and error bars indicate combined errors of averages).

yields of [Mn/Fe] that are seen in, e.g., the Milky Way thick disk (Feltzing et al. 2007).

As pointed out by Kirby et al. (2019), our conclusions are valid only for SNe Ia that occurred while Sculptor was forming stars. According to Weisz et al. (2014), Sculptor formed the middle two thirds of its stars in 1 Gyr. Our measurements are therefore sensitive to models of SNe Ia that have "standard" delay-times <0.6 Gyr (e.g., Maoz et al. 2014). However, our conclusions do not account for SNe Ia that are delayed by more than 1 Gyr. Measurements of other dSphs with different SFHs may be required to sample different varieties of SNe Ia, which may have longer delay times. We discuss this further in the next section.

5.2. Other dSph Galaxies

As described in Section 4.1, we are unable to fit our simple chemical evolution model to several dSphs. Ursa Minor, Ursa Major II, and Canes Venatici have small sample sizes; Leo I and Fornax dSphs have larger sample sizes (N = 50 and N = 45, respectively), but are not well fit by the model. For completeness, we illustrate the Mn abundances as a function of metallicity for all dSphs in the left panel of Figure 7.

The right panel of Figure 7 zooms in on [Mn/Fe] as a function of [Fe/H] for the galaxies with sample sizes N > 20: Sculptor, Leo I, and Fornax. This illustrates that at a given [Fe/H], stars in Leo I and Fornax have higher [Mn/Fe] abundances than stars in Sculptor by $\gtrsim 0.2$ dex on average.

The most obvious differences among these galaxies that might explain this discrepancy are the galaxies' SFHs. Leo I and Fornax have extended SFHs, while Sculptor's SFH is characterized by a burst of early star formation followed by a long period of low star formation rates. This may explain the difference in [Mn/Fe] between these galaxies. Here, we consider two potential reasons why SFH might be linked with [Mn/Fe] abundance.

First, differences in [Mn/Fe] at a given [Fe/H] may result from a combination of star formation timescales and metallicity-dependent SN Ia yields. Star formation timescales are relevant because this work uses *stellar* abundances, which trace the level of chemical enrichment at the time of star formation rather than the current level of enrichment. Thus, a star with [Fe/H] ~ -1.50 may actually be sampling yields produced by SNe Ia with

[Fe/H] < -1.50 progenitors. This "lag" in metallicity would be smaller in Leo I and Fornax than in Sculptor, because of their extended SFHs. If [Mn/Fe] yields from sub- M_{Ch} SNe Ia were metallicity-dependent—more specifically, if [Mn/Fe] yields were to increase as progenitor [Fe/H] increases—then the difference in [Mn/Fe] at a given [Fe/H] between Sculptor and Fornax/Leo I might simply be a result of the difference in "lag metallicity."

Although a full test of this hypothesis is beyond the scope of this work, to first order we can estimate the effect of this "lag" by computing the average delay time for SNe Ia in each dSph. We do this by assuming a power-law delay-time distribution (Maoz et al. 2012):

$$\Psi = 10^{-3} \left(\frac{t}{\text{Gyr}}\right)^{-1.1} \text{SNe Gyr}^{-1} M_{\odot}^{-1}.$$
 (8)

We assume that this delay-time distribution is valid only for times later than some minimum time $t_{\rm min} \sim 0.1$ Gyr. We can then compute the average delay time for SNe Ia between $t_{\rm min}$ and some typical star formation time t_* :

$$t_{\text{delay}} = \frac{\int_{t_{\text{min}}}^{t_*} t \Psi dt}{\int_{t_{\text{min}}}^{t_*} \Psi dt}.$$
 (9)

For Sculptor, de Boer et al. (2012) report that Sculptor formed most of its stars within a duration of \sim 7 Gyr. ¹³ We assume an average star formation time of $t_* \sim 3.5$ Gyr, which yields a delay time of $t_{\rm delay} \sim 0.87$ Gyr. Using the agemetallicity relation from de Boer et al. (2012), this corresponds to a metallicity lag of $\Delta {\rm [Fe/H]} \sim 0.2$ dex. Similarly, Letarte et al. (2010) report a typical star formation time of $t_* \sim 5$ Gyr for Fornax, corresponding to $t_{\rm delay} \sim 1.12$ Gyr. With Letarte et al.'s age-metallicity relation, this yields a metallicity lag of $\Delta {\rm [Fe/H]} \sim 0.15$ dex. Therefore, the difference in metallicity lags between Sculptor and Fornax is \sim 0.05 dex. For the S18

 $[\]overline{13}$ We note that this is a relatively extended SFH estimate. Weisz et al. (2014) find a much shorter SFH, suggesting that Sculptor formed most of its stars in ~ 1 Gyr. However, Weisz et al. (2014) do not publish an age-metallicity relation; for consistency we therefore use the SFH and age-metallicity relation from de Boer et al. (2012) for this order of magnitude calculation.

 $1\,M_\odot$ SNe Ia model, a ~ 0.05 dex difference in metallicity lags produces a difference in [Mn/Fe] of Δ [Mn/Fe] ~ 0.05 dex. This is not enough to explain the $\gtrsim 0.2$ dex difference in [Mn/Fe] between Sculptor and Fornax.

Alternatively, the discrepancy in [Mn/Fe] may result from a change over time in the underlying physical mechanism behind SNe Ia. Both Leo I and Fornax have stars with significantly super-solar [Mn/Fe] abundances ([Mn/Fe] $\gtrsim 0.2$ dex); as Figure 5 shows, low-metallicity sub- $M_{\rm Ch}$ Type Ia progenitors do not produce such high [Mn/Fe] yields. This suggests that near- $M_{\rm Ch}$ WD explosions may become the dominant channel for SNe Ia at late times in a galaxy's SFH.

Such a scenario—where near- $M_{\rm Ch}$ SNe Ia or SNe Iax explode later than sub- $M_{\rm Ch}$ SNe Ia—has been proposed by, e.g., Kobayashi & Nomoto (2009), who argue that near- $M_{\rm Ch}$ SNe Ia are suppressed at low metallicities due to metallicity-dependent WD winds. This scenario may also be consistent with near- $M_{\rm Ch}$ explosions requiring mass growth by hydrogen accretion, which may require a longer delay time or higher-metallicity progenitors than sub- $M_{\rm Ch}$ double-degenerate mergers (e.g., Ruiter et al. 2011). As noted in Section 4.2 this also agrees with observations in the Milky Way, which show that stars in the Galactic halo have sub-solar [Mn/Fe] at [Fe/H] $\lesssim -1.0$, compared to stars in the higher-metallicity thick disk, which have have super-solar [Mn/Fe] (Feltzing et al. 2007). Like Sculptor, the Milky Way halo formed most of its stars in a short early burst, while the thick disk has a more extended SFH.

5.3. NLTE Effects

Throughout our analysis, we have used [Mn/Fe] abundance measurements that rely on the assumption of LTE. In LTE, opacity is only a function of temperature and density. However, this is only valid at high densities, when the radiation field is strongly coupled to the matter. Previous works find that accounting for NLTE effects may systematically increase Mn abundances by as much as 0.5–0.7 dex using 1D NLTE models (e.g., Bergemann & Gehren 2008), or up to ~0.4 dex using 3D NLTE models (e.g., Bergemann et al. 2019). We must therefore consider the effect of NLTE corrections on our results.

We estimate this using the corrections determined by Bergemann & Gehren (2008), who compared Mn abundances measured using 1D LTE models and 1D NLTE models over a range of metallicities. From Figure 9 of Bergemann et al. (2019), we find that for a typical RGB star ($T_{\rm eff} = 6000$ K, log g = 1.5), 1D NLTE corrections ($\Delta_{\rm NLTE} = [{\rm Mn/Fe}]_{\rm NLTE} - [{\rm Mn/Fe}]_{\rm LTE})$ determined from optical lines used in this work range from $\Delta_{\rm NLTE} \lesssim 0.462$ dex at [Fe/H] = -3 to $\Delta_{\rm NLTE} \gtrsim 0.173$ dex at [Fe/H] = 0. By linearly interpolating between these bounds, we can determine a maximum "statistical" NLTE correction as a function of [Fe/H]¹⁴:

$$\Delta_{\text{NLTE}}([\text{Fe/H}]) = -0.10[\text{Fe/H}] + 0.17.$$
 (10)

Figure 8 shows the results of applying this maximum correction to our [Mn/Fe] measurements for stars in Sculptor

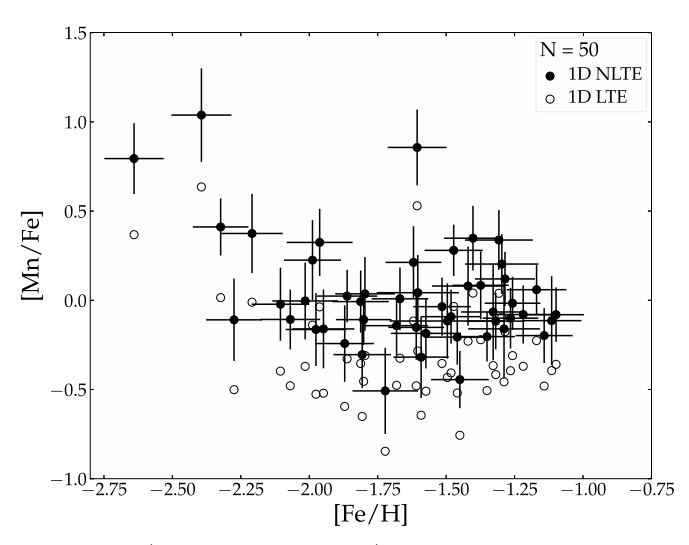


Figure 8. [Mn/Fe] as a function of [Fe/H] in Sculptor dSph. Filled points indicate the measurements with a statistical correction for 1D NLTE effects; empty points indicate the original 1D LTE measurements.

dSph. The 1D NLTE corrections have a very slight metallicity dependence, but their primary effect is to increase all of the [Mn/Fe] yields by a factor of \sim 0.33 dex on average. This naturally increases the [Mn/Fe] yields inferred from Sculptor dSph: [Mn/Fe]_{CC,NLTE} = $0.00^{+0.03}_{-0.03}$ for CCSNe, and [Mn/Fe]_{Ia,NLTE} = $+0.03^{+0.03}_{-0.03}$ at [Fe/H] = -1.5 dex for SNe Ia. This near-solar SN Ia yield is consistent with $M_{\rm Ch}$ theoretical models (see Figure 5), a significant departure from our finding in Section 5.1 that the sub- $M_{\rm Ch}$ channel dominates in Sculptor dSph. Furthermore, Bergemann et al. (2019) suggest that 3D effects, such as convection, may further increase [Mn/Fe] abundances in RGB stars by another \sim 0.2 dex, producing an even higher [Mn/Fe]_{Ia} yield.

This is an interesting difference with respect to our LTE estimates. However, we will leave this complex analysis including detailed NLTE to a future study, ¹⁵ since Kirby et al. (2018) found that applying 1D NLTE corrections instead increased the dispersion of Fe-peak abundances ([Co/Fe] and [Cr/Fe]) in globular clusters. Kirby et al. suggested that this behavior is due to the method by which the atmospheric parameters were determined (1D LTE modeling of spectra with a microturbulence relationship calibrated on LTE results).

In any case, the NLTE corrections do not appear to strongly affect the metallicity dependence of [Mn/Fe]; as in the LTE case, we observe a nearly flat trend of [Mn/Fe] versus [Fe/H] across the metallicity range -2.25 < [Fe/H] < -1.0 in Sculptor. Furthermore, our comparison between Sculptor and other dSph galaxies (Leo I, Fornax) depends primarily on relative differences between [Mn/Fe] abundances at a given [Fe/H]. Effective temperature might also affect the magnitude of NLTE corrections, but $T_{\rm eff}$ at a given [Fe/H] in Sculptor, Leo I, and Fornax are offset by 200–300 K at most; the resulting difference in NLTE corrections is \leq 0.05 dex, not enough to explain the discrepancy in [Mn/Fe] at a given [Fe/H] between these galaxies. NLTE corrections are therefore unlikely to affect our interpretation of [Mn/Fe] abundances as a function of SFH (Section 5.2).

 $[\]overline{^{14}}$ We note that although we consider primarily NLTE effects on Mn I lines, NLTE conditions can also affect Fe I lines. Predictions for NLTE Fe I corrections can be quite large (up to 0.5 dex; see, e.g., Bergemann et al. 2012, 2017; Mashonkina et al. 2019). However, these large corrections are generally applicable for metal-poor stars with $[Fe/H] \lesssim -2.0$. For cool giant stars with metallicities comparable to the bulk of our sample [Fe/H] > -2.0, Mashonkina et al. (2019) predict NLTE corrections \lesssim 0.1 dex (see their Figure 8). This change is smaller than the average NLTE corrections predicted by Equation (10).

 $[\]overline{^{15}}$ This requires a complete re-analysis of stellar parameters of our targets using NLTE models.

6. Summary and Conclusions

We have presented the results of MRS from the new 1200B grating on Keck DEIMOS. Using a pipeline that generates synthetic stellar spectra, we have measured Mn abundances for N = 161 stars in six classical dSph galaxies. These Mn abundance measurements were validated using the internal dispersions of globular clusters and comparison with high-resolution spectroscopy.

By fitting a simple chemical evolution model to measurements of [Mn/Fe] as a function of [Fe/H], we have inferred the Mn yields of CCSNe and early SNe Ia in Sculptor dSph: $[Mn/Fe]_{CC} = -0.33^{+0.03}_{-0.03}$ and $[Mn/Fe]_{Ia} = -0.30^{+0.03}_{-0.03}$ (at [Fe/H] = -1.5), respectively. Since only sub- M_{Ch} SN Ia models are able to produce significantly sub-solar values of $[Mn/Fe]_{Ia}$, we conclude that the dominant explosion mechanism of SNe Ia that occurred before the end of star formation in Sculptor is the detonation of a sub- M_{Ch} WD. However, in order to reproduce our observationally inferred $[Mn/Fe]_{Ia}$, we find that a fraction ($\gtrsim 20\%$) of all SNe Ia in our metallicity range -2 < [Fe/H] < -1 must have near- M_{Ch} progenitors.

This conclusion may not hold for other environments. In particular, the Milky Way thick disk and dSphs with extended SFHs display different trends of [Mn/Fe] as a function of metallicity. We find that, at a given metallicity, dSphs with extended SFHs like Fornax and Leo I have $\gtrsim 0.2$ dex higher average [Mn/Fe] abundances than Sculptor, which has an ancient SFH. This discrepancy is large enough to imply a physical change in the nucleosynthetic source of Mn; perhaps the dominant channel of SNe Ia evolves over time, and near- $M_{\rm Ch}$ WD detonations become the dominant channel at longer delay times.

Finally, we consider the effect of NLTE corrections on our results. Including a statistical NLTE correction increases the [Mn/Fe] yields from both CCSNe and SNe Ia by \sim 0.3 dex. The resulting [Mn/Fe] $_{\rm Ia}$ is approximately solar at [Fe/H] \sim -1.5, more consistent with yields from near- $M_{\rm Ch}$ models. The detailed treatment of NLTE effects, however, requires a full re-analysis of stellar parameters of our targets with NLTE synthetic spectral models. This will be the subject of future work.

We also hope to test the results of this work using more data in dSphs. Other dSphs with ancient SFHs similar to Sculptor (e.g., Draco, Canes Venatici II) could be used to confirm whether sub- $M_{\rm Ch}$ explosions dominate at early times in dwarf galaxies. dSph galaxies with diverse SFHs, such as Carina (e.g., Hernandez et al. 2000), may also be particularly intriguing environments in which to test our conclusions about the SFH dependence of SNe Ia.

The authors thank I. Escala and G. Duggan for informing parts of the data pipeline, as well as A. Piro and A. McWilliam for helpful discussions and comments. This material is based upon work supported by the National Science Foundation under grant No. AST-1847909. M.A.dl.R. acknowledges the financial support of the NSF Graduate Research Fellowship Program. E.N.K. gratefully acknowledges support from a Cottrell Scholar award administered by the Research Corporation for Science Advancement as well as funding from generous donors to the California Institute of Technology. I.R.S. was supported by the Australian Research Council through grant No. FT160100028.

The authors wish to recognize and acknowledge the deep cultural role and reverence that the summit of Maunakea has always had within the indigenous Hawaiian community. We are most fortunate to have the opportunity to conduct

observations from this sacred mountain. Finally, we would like to express our deep gratitude to the staff at academic and telescope facilities, particularly those whose communities are excluded from the academic system, but whose labor maintains spaces for scientific inquiry.

Facility: Keck:II (DEIMOS).

Software: spec2d (Cooper et al. 2012; Newman et al. 2013), Matplotlib (Hunter 2007), Astropy (Robitaille et al. 2013), Scipy (Jones et al. 2001), MOOG (Sneden et al. 2012), ATLAS9 (Castelli & Kurucz 2003).

Appendix Theoretical Yield Tables

In this section, we briefly describe the theoretical models of SNe Ia. These models are discussed in further detail in Section 4.1 of Kirby et al. (2019). Tables 9 and 10 list the theoretical [Mn/Fe] yields predicted by the $M_{\rm Ch}$ and sub- $M_{\rm Ch}$ models, respectively. Here we discuss the details of [Mn/Fe] predictions from these models.

A.1. Deflagration-to-detonation

We consider two sets of near-M_{Ch} DDT models. Since the burning front is highly textured, we chose only multi-dimensional simulations.

DDT(S13): S13 produced 3D models of CO WDs with varying numbers of off-center ignition sites, which are

Table 9 Theoretical Yields for M_{Ch} Models

Model	$\log(Z/Z_{\odot})$	[Mn/Fe]
	DDT(S13)	
N1	0.0	+0.01
N3	0.0	-0.06
N10	0.0	+0.01
N100	-0.5	+0.27
N200	0.0	+0.50
N1600	0.0	+0.53
	def(F14)	
N1def	0.0	+0.36
N3def	0.0	+0.42
N10def	0.0	+0.44
N100def	0.0	+0.48
N200def	0.0	+0.50
N1600def	0.0	+0.52
	DDT(L18)	
*WDD2	0.0	+0.15
DDT $1 \times 10^9 \text{ g cm}^{-3}$	-0.5	-0.17
DDT $3 \times 10^9 \text{ g cm}^{-3}$	-0.5	+0.14
DDT $5 \times 10^9 \text{ g cm}^{-3}$	-0.5	+0.30
	def(L18)	
*W7	-0.5	+0.30
$\mathrm{def}1\times10^9~\mathrm{g~cm^{-3}}$	0.0	+0.19
$def 3 \times 10^9 \text{ g cm}^{-3}$	0.0	+0.39
$def 5 \times 10^9 \text{ g cm}^{-3}$	0.0	+0.39

Note

^a In this table and in Table 10, models marked with asterisks (*) are "special cases" denoted with dashed lines in Figure 5.

Table 10 Theoretical Yields for Sub- M_{Ch} Models

Model	$\log(Z/Z_{\odot})$	[Mn/Fe]
	sub(L19)	
$0.90 M_{\odot}, M_{\rm He} = 0.15 M_{\odot}$	0.0	+0.25
$0.95 M_{\odot}, M_{\rm He} = 0.15 M_{\odot}$	0.0	-0.13
$1.00 M_{\odot}, M_{\text{He}} = 0.10 M_{\odot}$	0.0	-0.23
$1.05 M_{\odot}, M_{\text{He}} = 0.10 M_{\odot}$	0.0	-0.25
$^*1.10 M_{\odot}, M_{\text{He}} = 0.10 M_{\odot}$	-1.5	-0.44
$1.15 M_{\odot}, M_{\text{He}} = 0.10 M_{\odot}$	0.0	-0.45
$1.20 M_{\odot}, M_{\text{He}} = 0.05 M_{\odot}$	0.0	-0.34
	sub(S18)	
$0.85 M_{\odot}, \text{C/O} = 50/50$	-1.5	-0.64
$0.90 M_{\odot}, C/O = 50/50$	-1.5	-0.75
$1.00 M_{\odot}, \text{C/O} = 50/50$	-1.5	-1.05
$1.10 M_{\odot}, C/O = 50/50$	-1.5	-1.33
$^*0.85 M_{\odot}, C/O = 30/70$	-1.5	-0.55
$^*0.90 M_{\odot}, \text{C/O} = 30/70$	-1.5	-0.73
*1.00 M_{\odot} , C/O = 30/70	-1.5	-1.00
*1.10 M_{\odot} , C/O = 30/70	-1.5	-1.26
	sub(B19)	
$0.88 M_{\odot}, \xi_{\rm CO} = 0.9$	-1.5	-0.55
$0.97 M_{\odot}, \xi_{\rm CO} = 0.9$	-1.5	-0.81
$1.06 M_{\odot}, \xi_{\rm CO} = 0.9$	-1.5	-1.16
$1.10 M_{\odot}, \xi_{\rm CO} = 0.9$	-1.5	-1.28
$1.15 M_{\odot}, \xi_{\rm CO} = 0.9$	-1.5	-1.42
$^*0.88 M_{\odot}, \xi_{\rm CO} = 0.0$	-1.5	-0.50
*0.97 M_{\odot} , $\xi_{\rm CO} = 0.0$	-1.5	-0.81
$^*1.06 M_{\odot}, \xi_{\rm CO} = 0.0$	-1.5	-1.16
$^*1.10 M_{\odot}, \xi_{\rm CO} = 0.0$	-1.5	-1.28
*1.15 M_{\odot} , $\xi_{\rm CO} = 0.0$	-1.5	-1.42

specified in the model names; e.g., N10 has 10 ignition sites. More ignition sites correspond to stronger deflagration phases where ⁵⁵Mn (or rather, its parent nucleus ⁵⁵Co) is produced, producing higher [Mn/Fe] yields.

DDT(L18): L18 computed 2D models with single central ignition points and a variety of central densities. As described in Section 1.2, Mn yields increase with density in near- $M_{\rm Ch}$ WDs. We also consider L18's model "WDD2," the classic DDT model of Iwamoto et al. (1999) updated with new electron capture rates.

We note that both S13 and L18 ran solar-metallicity and low-metallicity models. However, their low-metallicity models do not include "simmering," pre-explosion convective burning in the cores of near- $M_{\rm Ch}$ progenitors. Simmering may increase the neutron excess (e.g., Piro & Bildsten 2008; Chamulak et al. 2008), effectively making the initial metallicity of a $M_{\rm Ch}$ SN Ia irrelevant below a threshold of $\sim 1/3-2/3Z_{\odot}$ (Piro & Bildsten 2008; Martínez-Rodríguez et al. 2016). Since our most metal-rich stars are well below this threshold metallicity, when possible we interpolate the DDT models to a threshold metallicity of $\sim 1/3Z_{\odot}$.

A.2. Pure Deflagration

We consider two sets of pure deflagrations of near-M_{Ch} WDs. These may represent SNe Iax (e.g., Kromer et al. 2015),

so their nucleosynthetic yields may not be applicable to "normal" SNe Ia.

def(F14): F14 produced 3D models that closely paralleled the DDT models of S13 and varied the number of off-center sites of ignition. As with S13, the number of ignition sites increases with the strength of the deflagration, increasing the [Mn/Fe] yields.

def(L18): L18 computed pure deflagrations that paralleled the initial central densities as their DDT models. As with the DDT models, Mn yields increase with density. L18 also updated the pure-deflagration "W7" model of Iwamoto et al. (1999).

A.3. Sub- M_{Ch}

We consider three sets of sub- $M_{\rm Ch}$ models. Each set considers a range of sub- $M_{\rm Ch}$ WD masses, and within each set the [Mn/Fe] yield tends to decrease with increasing WD mass. This is because, as mentioned in Section 1.2, in low-mass WDs ($\lesssim 1.2\,M_{\odot}$) ⁵⁵Co is produced at densities below nuclear statistical equilibrium. As a result, the ⁵⁵Co yield (and therefore the ⁵⁵Mn yield) does not change drastically as a function of mass. Meanwhile, the ⁵⁶Ni mass does increase with mass; since ⁵⁶Ni is the parent nucleus of most stable Fe, the overall [Mn/Fe] ratio decreases with mass.

sub(L19): L19 used the same 2D code as their earlier work in L18. All L19 models were computed at solar metallicity, except for the $1.10~M_{\odot}$ ("benchmark") model, which we consider at [Fe/H] ~ -1.5 for ease of comparison with the observationally inferred yields.

sub(S18): \$18 simulated 1D detonations of CO sub- $M_{\rm Ch}$ WDs. We again consider only models interpolated to a metallicity of [Fe/H] ~ -1.5 to better compare against our observations. They simulated C/O mass ratios of both 50/50 and 30/70, which is more physically representative of the C/O ratio in actual WDs.

sub(B19): B19 also simulated 1D detonations starting at the centers of sub- $M_{\rm Ch}$ WDs. They explored the effect of reducing the reaction rate of $^{12}{\rm C}$ + 16 O by a factor of 10; these reduced reaction rate models are represented by $\xi_{\rm CO}=0.9$ in Table 10, while models with the "standard" reaction rate have $\xi_{\rm CO}=0.0$.

ORCID iDs

Mithi A. C. de los Reyes https://orcid.org/0000-0002-4739-046X

Evan N. Kirby https://orcid.org/0000-0001-6196-5162
Ivo R. Seitenzahl https://orcid.org/0000-0002-5044-2988
Ken J. Shen https://orcid.org/0000-0002-9632-6106

References

Abohalima, A., & Frebel, A. 2018, ApJS, 238, 36
Arnett, W. D., Truran, J. W., & Woosley, S. E. 1971, ApJ, 165, 87
Asplund, M., Grevesse, N., Sauval, A. J., & Scott, P. 2009, ARA&A, 47, 481
Baumgardt, H., & Hilker, M. 2018, MNRAS, 478, 1520
Bergemann, M., Collet, R., Schönrich, R., et al. 2017, ApJ, 847, 16
Bergemann, M., Gallagher, A. J., Eitner, P., et al. 2019, A&A, 631, A80
Bergemann, M., & Gehren, T. 2008, A&A, 492, 823
Bergemann, M., Lind, K., Collet, R., Magic, Z., & Asplund, M. 2012, MNRAS, 427, 27
Bonifacio, P., Spite, M., Cayrel, R., et al. 2009, A&A, 501, 519
Bravo, E., Badenes, C., & Martínez-Rodríguez, H. 2019, MNRAS, 482, 4346

Carretta, E., Bragaglia, A., Gratton, R. G., et al. 2010, A&A, 520, A95
Castelli, F., & Kurucz, R. L. 2003, in IAU Symp. 210, ed. N. Piskunuv,
W. W. Weiss, & D. F. Gray (San Francisco, CA: ASP), A20

```
Cescutti, G., & Kobayashi, C. 2017, A&A, 607, A23
Chamulak, D. A., Brown, E. F., Timmes, F. X., & Dupczak, K. 2008, ApJ,
   677, 160
Cooper, M. C., Newman, J. A., Davis, M., Finkbeiner, D. P., & Gerke, B. F.
   2012, spec2d: DEEP2 DEIMOS Spectral Pipeline, v.1.1.4, Astrophysics
   Source Code Library, ascl:1203.003
Cunha, K., Smith, V. V., Bergemann, M., Suntzeff, N. B., & Lambert, D. L.
   2010, ApJ, 717, 333
de Boer, T. J. L., Tolstoy, E., Hill, V., et al. 2012, A&A, 539, A103
Duggan, G. E., Kirby, E. N., Andrievsky, S. M., & Korotin, S. A. 2018, ApJ,
Escala, I., Kirby, E. N., Gilbert, K. M., Cunningham, E. C., & Wojno, J. 2019,
    ApJ, 878, 42
Faber, S. M., Phillips, A. C., Kibrick, R. I., et al. 2003, Proc. SPIE, 4841, 1657
Feltzing, S., Fohlman, M., & Bensby, T. 2007, A&A, 467, 665
Fink, M., Kromer, M., Seitenzahl, I. R., et al. 2014, MNRAS, 438, 1762
Foreman-Mackey, D., Hogg, D. W., Lang, D., & Goodman, J. 2013, PASP,
Frebel, A., Simon, J. D., Geha, M., & Willman, B. 2010, ApJ, 708, 560
Giammichele, N., Bergeron, P., & Dufour, P. 2012, ApJS, 199, 29
Gustafsson, B., Bell, R. A., Eriksson, K., & Nordlund, A. 1975, A&A, 500, 67
Gustafsson, B., Edvardsson, B., Eriksson, K., et al. 2003, in ASP Conf. Ser. 288,
   Stellar Atmosphere Modeling, ed. I. Hubeny, D. Mihalas, & K. Werner
   (San Francisco, CA: ASP), 697
Gustafsson, B., Edvardsson, B., Eriksson, K., et al. 2008, A&A, 486, 951
Harris, W. E. 1996, AJ, 112, 1487
Hernandez, X., Gilmore, G., & Valls-Gabaud, D. 2000, MNRAS, 317, 831
Hogg, D. W., Bovy, J., & Lang, D. 2010, arXiv:1008.4686
Hunter, J. D. 2007, CSE, 9, 90
Iben, I., & Tutukov, A. V. 1984, ApJS, 54, 335
Iwamoto, K., Brachwitz, F., Nomoto, K., et al. 1999, ApJS, 125, 439
Johnson, C. I., & Pilachowski, C. A. 2010, ApJ, 722, 1373
Jones, E., Oliphant, T., Peterson, P., et al. 2001, SciPy: Open Source Scientific
   Tools for Python, www.scipy.org/
Khokhlov, A. 1991, A&A, 245, 114
Kirby, E. N., Guhathakurta, P., Bolte, M., Sneden, C., & Geha, M. C. 2009,
    ApJ, 705, 328
Kirby, E. N., Guhathakurta, P., Simon, J. D., et al. 2010, ApJS, 191, 352
Kirby, E. N., Guhathakurta, P., Zhang, A. J., et al. 2016, ApJ, 819, 135
Kirby, E. N., Xie, J. L., Guo, R., et al. 2019, ApJ, 881, 45
Kirby, E. N., Xie, J. L., Guo, R., Kovalev, M., & Bergemann, M. 2018, ApJS,
   237, 18
Kobayashi, C., & Nomoto, K. 2009, ApJ, 707, 1466
Kobayashi, C., Nomoto, K., & Hachisu, I. 2015, ApJL, 804, L24
Kramida, A., Ralchenko, Y., Reader, J. & NIST ASD Team 2014, NIST
   Atomic Spectra Database, v. 5.2, (Gaithersburg, MD: NIST)
Kromer, M., Ohlmann, S. T., Pakmor, R., et al. 2015, MNRAS, 450, 3045
Kurucz, R. 1993, SYNTHE spectrum synthesis programs and line data CD-
   ROM (Cambridge, MA: Smithsonian Astronophysical Observatory), 13
Lardo, C., Pancino, E., Mucciarelli, A., et al. 2013, MNRAS, 433, 1941
Lesaffre, P., Han, Z., Tout, C. A., Podsiadlowski, P., & Martin, R. G. 2006,
   MNRAS, 368, 187
Letarte, B., Hill, V., Tolstoy, E., et al. 2010, A&A, 523, A17
```

```
Leung, S.-C., & Nomoto, K. 2018, ApJ, 861, 143
Leung, S.-C., & Nomoto, K. 2020, ApJ, 888, 80
Livne, E. 1990, ApJL, 354, L53
Maoz, D., Mannucci, F., & Brandt, T. D. 2012, MNRAS, 426, 3282
Maoz, D., Mannucci, F., & Nelemans, G. 2014, ARA&A, 52, 107
Margutti, R., Soderberg, A. M., Chomiuk, L., et al. 2012, ApJ, 751, 134
Martínez-Rodríguez, H., Piro, A. L., Schwab, J., & Badenes, C. 2016, ApJ,
Mashonkina, L., Sitnova, T., Yakovleva, S. A., & Belyaev, A. K. 2019, A&A,
  631, A43
Massari, D., Mucciarelli, A., Ferraro, F. R., et al. 2014, ApJ, 791, 101
McConnachie, A. 2012, AJ, 144, 4
McWilliam, A., Piro, A. L., Badenes, C., & Bravo, E. 2018, ApJ, 857, 97
Newman, J. A., Cooper, M. C., Davis, M., et al. 2013, ApJS, 208, 5
Nomoto, K. 1982, ApJ, 257, 780
North, P., Cescutti, G., Jablonka, P., et al. 2012, A&A, 541, 45
Pancino, E., Mucciarelli, A., Sbordone, L., et al. 2011, A&A, 527, A18
Pérez-Torres, M. A., Lundqvist, P., Beswick, R. J., et al. 2014, ApJ, 792, 38
Perlmutter, S., Aldering, G., Goldhaber, G., et al. 1999, ApJ, 517, 565
Phillips, M. M. 1993, ApJL, 413, L105
Piro, A. L., & Bildsten, L. 2008, ApJ, 673, 1009
Riess, A. G., Filippenko, A. V., Challis, P., et al. 1998, AJ, 116, 1009
Robitaille, T. P., Tollerud, E. J., Greenfield, P., et al. 2013, A&A, 558, A33
Ruiter, A. J., Belczynski, K., Sim, S. A., et al. 2011, MNRAS, 417, 408
Seitenzahl, I. R., Cescutti, G., Röpke, F. K., Ruiter, A. J., & Pakmor, R. 2013a,
   A&A, 559, L5
Seitenzahl, I. R., Ciaraldi-Schoolmann, F., Röpke, F. K., et al. 2013b,
  MNRAS, 429, 1156
Seitenzahl, I. R., Kromer, M., Ohlmann, S. T., et al. 2016, A&A, 592, A57
Seitenzahl, I. R., Summa, A., Krauß, F., et al. 2015, MNRAS, 447, 1484
Seitenzahl, I. R., Taubenberger, S., & Sim, S. A. 2009, MNRAS, 400, 531
Seitenzahl, I. R., & Townsley, D. M. 2017, in Handbook of Supernovae, ed.
   A. Alsabti & P. Murdin (Cham: Springer), 1
Shen, K. J., & Bildsten, L. 2007, ApJ, 660, 1444
Shen, K. J., Boubert, D., Gänsicke, B. T., et al. 2018a, ApJ, 865, 15
Shen, K. J., Kasen, D., Miles, B. J., & Townsley, D. M. 2018b, AJ, 854, 52
Shetrone, M., Venn, K. A., Tolstoy, E., et al. 2003, AJ, 125, 684
Simon, J. D., & Geha, M. 2007, ApJ, 670, 313
Sneden, C., Bean, J., Ivans, I., Lucatello, S., & Sobeck, J. 2012, MOOG: LTE
  line analysis and spectrum synthesis, v2017, Astrophysics Source Code
  Library, ascl:1202.009
Sneden, C., Cowan, J. J., Kobayashi, C., et al. 2016, ApJ, 817, 53
Sneden, C., Kraft, R. P., Shetrone, M. D., et al. 1997, AJ, 114, 1964
Sobeck, J. S., Ivans, I. I., Simmerer, J. A., et al. 2006, AJ, 131, 2949
Sobeck, J. S., Kraft, R. P., Sneden, C., et al. 2011, AJ, 141, 175
Spite, M. 1967, AnAp, 30, 211
Tremblay, P.-E., Cummings, J., Kalirai, J. S., et al. 2016, MNRAS, 461, 2100
Webbink, R. F. 1984, ApJ, 277, 355
Weisz, D. R., Dolphin, A. E., Skillman, E. D., et al. 2014, ApJ, 789, 147
Woosley, S. E., & Kasen, D. 2011, ApJ, 734, 38
Woosley, S. E., Taam, R. E., & Weaver, T. A. 1986, ApJ, 301, 601
Yamaguchi, H., Badenes, C., Foster, A. R., et al. 2015, ApJL, 801, L31
Yong, D., Roederer, I. U., Grundahl, F., et al. 2014, MNRAS, 441, 3396
```